Advances in Silica Planar Lightwave Circuits

Christopher Richard Doerr, *Member, IEEE*, and Katsunari Okamoto, *Fellow, IEEE*

Invited Paper

Abstract—This paper presents a synopsis of some of the advances in silica waveguide planar lightwave circuits (PLCs). It concentrates on silica PLCs for fiber-optic communications, mainly routing and signal processing devices. A significant portion is devoted to arrayed waveguide gratings.

Index Terms—Gratings, integrated optics, optical equalizers, optical fibers, optical planar waveguide components, optical planar waveguide couplers, optical planar waveguides.

I. INTRODUCTION

THIS PAPER summarizes some of the progress and understanding of optical devices made in silica waveguide planar lightwave circuits (PLCs). Silica waveguide PLCs typically consist of a planar arrangement of glass waveguides with a higher index of refraction buried in glass all on a silicon or glass substrate. Silica waveguide PLCs have enjoyed significant success in optical fiber communications because of their reliability, low insertion loss, ease of coupling to optical fibers, integration capability, and ability to produce optical filters with high accuracy.

The market for silica waveguide PLCs is dominated by simple optical couplers/splitters with a recent surge in sales due to fiber-to-the-home deployments. However, sales of arrayed waveguide grating (AWG) wavelength de/multiplexers, a much more complex device than a simple coupler/splitter, have been increasing significantly since the late 1990s. AWG performance can now exceed that of thin-film filter-based de/multiplexers, and their manufacturing cost is lower. AWGs are one of the first examples of optical integration living up to the promise of eliminating most of the painstaking hand assembly from optical devices. More recently, even more complex devices, i.e., AWGs with switches and variable optical attenuators (VOAs) to act as multiplexers with channel power control (VMUXs) and reconfigurable optical add–drop multiplexers (ROADMs), have seen successful in the market. These are intersignal control devices. Intrasignal control devices, such as optical equalizers (which include dispersion compensators), pulse shapers, and demodulators, have not had market success yet but may soon.

C. R. Doerr is with Lucent Technologies, Bell Laboratories, Holmdel, NJ 07733 USA (e-mail: crdoerr@lucent.com).

K. Okamoto is with the Department of Electrical and Computer Engineering, University of California, Davis, CA 95616 USA (e-mail: katsu@okamoto-lab.com).
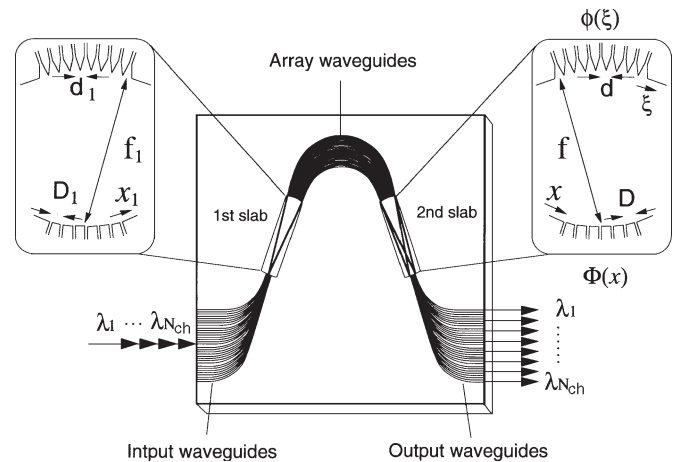
Fig. 1. Schematic configuration of AWG multiplexer.

This paper is designed mainly as a tutorial. It gives both a broad overview and a detailed discussion on some fundamental topics. The first part of this paper discusses mainly AWG fundamentals. Then, more complex PLC devices are discussed. Devices that perform both intersignal control and intrasignal control are discussed. Finally, there is a conclusion about where silica waveguide PLCs may be headed in the future.

II. OPTICAL FILTERING/MULTIPLEXING DEVICES

A highly successful method for constructing optical filters in PLCs is to use interferometers. An interferometer consisting of two couplers connected by two waveguides is called a Mach–Zehnder interferometer (MZI). An interferometer with more than two waveguides connecting two couplers is called an AWG. Other names for AWGs are PHASARs (phased arrays) and waveguide grating routers.

A. Principle of Operation and Fundamental Characteristics of AWGs

An $N \times N$ AWG multiplexer is very attractive in optical wavelength-division multiplexing (WDM) networks since it is capable of increasing the aggregate transmission capacity of a single strand of optical fiber [1]–[3]. The AWG consists of input/output waveguides, two focusing slab regions, and a phased array of multiple channel waveguides with a constant path length difference ΔL between neighboring waveguides (Fig. 1). In the first slab region, the input waveguide separation is D_1, the array waveguide separation is d_1, and the radius of curvature is f_1. Generally, the waveguide parameters in the first
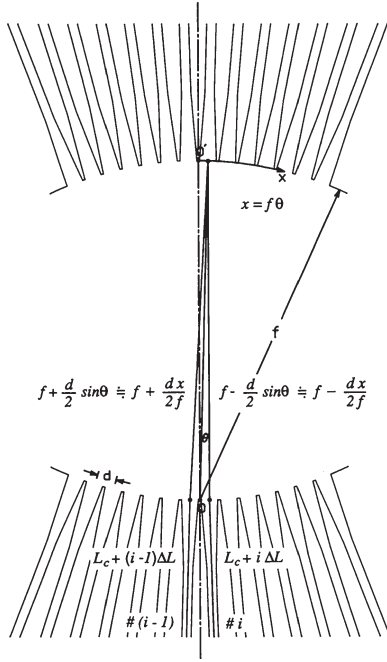
Fig. 2.   Enlarged view of the second slab region (rotated 180° from Fig. 1).

and second slab regions may be different. Therefore, in the second slab region, the output waveguide separation is D, the array waveguide separation is d, and the radius of curvature is f. The input light at position x_1 (x_1 is measured in a counterclockwise direction from the center of input waveguides) is radiated to the first slab and then excites the arrayed waveguides. The excited electric field amplitude in each array waveguide is a_i ($i = 1 - N$), where N is the total number of array waveguides. The amplitude profile a_i is usually a Gaussian distribution. After traveling through the arrayed waveguides, the light beams constructively interfere into one focal point x (x is measured in a counterclockwise direction from the center of output waveguides) in the second slab. The location of this focal point depends on the signal wavelength since the relative phase delay in each waveguide is given by $\Delta L / \lambda$. Fig. 2 shows an enlarged view of the second slab region. Let us consider the phase retardations for the two light beams passing through the $(i-1)$th and ith array waveguides. The geometrical distances of two beams in the second slab region are approximated as shown in Fig. 2. We have similar configurations in the first slab region as those in Fig. 2. The difference of the total phase retardations for the two light beams passing through the $(i-1)$th and ith array waveguides must be an integer multiple of 2π in order that the two beams constructively interfere at the focal point x. Therefore, we have the interference condition expressed by

$$\beta_s(\lambda_0)\left(f_1 - \frac{d_1 x_1}{2f_1}\right) + \beta_c(\lambda_0)[L_c + (i-1)\Delta L] + \beta_s(\lambda_0)\left(f + \frac{dx}{2f}\right)$$

$$= \beta_s(\lambda_0)\left(f_1 + \frac{d_1 x_1}{2f_1}\right) + \beta_c(\lambda_0)[L_c + i\Delta L]$$

$$+ \beta_s(\lambda_0)\left(f - \frac{dx}{2f}\right) - 2m\pi \qquad (1)$$

where β_s and β_c denote the propagation constants in the slab region and the array waveguide, respectively, m is an integer, λ_0 is the center wavelength of the WDM system, and L_c is the minimum array waveguide length. Subtracting common terms from (1), we obtain

$$\beta_s(\lambda_0)\frac{d_1 x_1}{f_1} - \beta_s(\lambda_0)\frac{dx}{f} + \beta_c(\lambda_0)\Delta L = 2m\pi. \qquad (2)$$

When the condition $\beta_c \lambda_0 \Delta L = 2m\pi$ or

$$\lambda_0 = \frac{n_c \Delta L}{m} \qquad (3)$$

is satisfied for λ_0, the light input position x_1 and the output position x should satisfy the condition

$$\frac{d_1 x_1}{f_1} = \frac{dx}{f}. \qquad (4)$$

In (3), n_c is the effective index of the array waveguide ($2\pi n_c = \beta_c / k$ k: wavenumber in vacuum), and m is called the diffraction order. The above equation means that when light is coupled into the input position x_1, the output position x is determined by (4). Usually, the waveguide parameters in the first and second slab regions are the same ($d_1 = d$ and $f_1 = f$). Therefore, the input and output distances are equal as $x_1 = x$. The spatial dispersion of the focal position x with respect to the wavelength λ for the fixed light input position x_1 is given by differentiating (2) with respect to λ as

$$\frac{\Delta x}{\Delta \lambda} = -\frac{N_c f \Delta L}{n_s d \lambda_0} \qquad (5)$$

where n_s is the effective index in the slab region, and N_c is the "group" index of the effective index n_c of the array waveguide ($N_c = n_c - \lambda dn_c / d\lambda$). The spatial dispersion of the input side position x_1 with respect to the wavelength λ for fixed light output position x is given by

$$\frac{\Delta x_1}{\Delta \lambda} = \frac{N_c f_1 \Delta L}{n_s d_1 \lambda_0}. \qquad (6)$$

The input and output waveguide separations are $|\Delta x_1| = D_1$ and $|\Delta x| = D$, respectively, when $\Delta \lambda$ is the channel spacing of the WDM signal. Putting these relations into (5) and (6), the wavelength spacing on the output side for a fixed light input position x_1 is given by

$$\Delta \lambda_{\text{out}} = \frac{n_s d D \lambda_0}{N_c f \Delta L} \qquad (7)$$
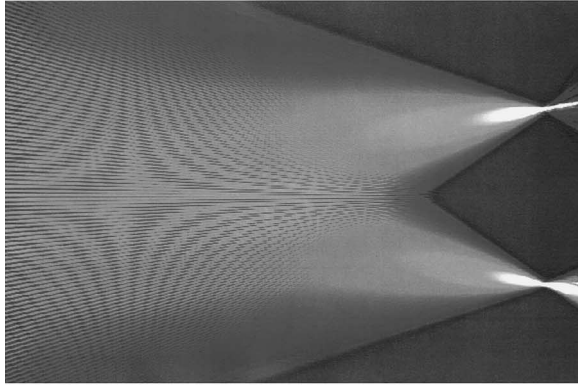
and the wavelength spacing on the input side for a fixed light output position x is given by

$$\Delta \lambda_{\text{in}} = \frac{n_s d_1 D_1 \lambda_0}{N_c f_1 \Delta L}. \qquad (8)$$

Often, the waveguide parameters in the first and second slab regions are the same, i.e., $D_1 = D$, $d_1 = d$, and $f_1 = f$. Then,
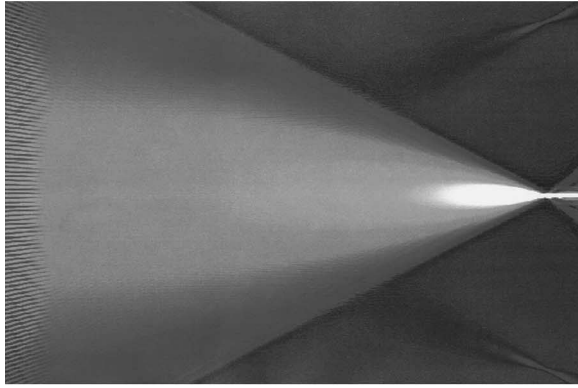
(a)

(b)

Fig. 3. BPM simulation of the light-focusing property in the second slab region (rotated $-90°$ from Fig. 1) for the (a) central wavelength λ_0 and (b) shorter wavelength component $\lambda < \lambda_0$.

the channel spacings are the same as $\Delta\lambda_{\text{in}} = \Delta\lambda_{\text{out}} \equiv \Delta\lambda$. The path length difference ΔL is obtained from (7) or (8) as

$$\Delta L = \frac{n_s dD\lambda_0}{N_c f \Delta\lambda}. \tag{9}$$

The spatial separation of the mth and $(m+1)$th focused beams for the same wavelength is given from (2) as

$$X_{\text{FSR}} = x_m - x_{m+1} = \frac{\lambda_0 f}{n_s d} \tag{10}$$

where X_{FSR} represents the free "spatial" range of the AWG. The number of available wavelength channels N_{ch} is given by dividing X_{FSR} with the output waveguide separation D as

$$N_{\text{ch}} = \frac{X_{\text{FSR}}}{D} = \frac{\lambda_0 f}{n_s dD}. \tag{11}$$

Fig. 3(a) and (b) shows a beam propagation method (BPM) simulation of the light-focusing property in the second slab region for the (a) central wavelength λ_0 and (b) a shorter wavelength component $\lambda < \lambda_0$. For the signal component which converges into the off-center output port as in Fig. 3(b), higher- or lower-order diffraction beams appear. Since one of the two diffraction beams in Fig. 3(b) is usually thrown away, the insertion loss for the peripheral output port becomes 2–3 dB higher than that for the central output port.

For further reading on AWG fundamentals, see [4]–[6] and [10].

B. Gaussian Spectral Response AWG

A "Gaussian" AWG denotes that the frequency response has a Gaussian shape. Various kinds of multiplexers including a 50-nm-spacing eight-channel AWG and a 25-GHz-spacing 400-channel AWG have been fabricated [7]–[9].

Fig. 4 shows the measured transmission spectra of a 32-channel 50-GHz-spacing AWG over four diffraction orders. As explained by the BPM simulations in Fig. 3(a) and (b), insertion losses for the peripheral output ports are 2.5–3 dB higher than those for central output ports. In order to obtain uniform loss characteristics in WDM system applications, the total number of channels N_{ch} of AWG should be significantly larger than the channel number N_{system} of the system. The number of output ports N_{system} is usually $0.5-0.6 \times N_{\text{ch}}$ to guarantee a loss variation of less than 1 dB.

Fig. 5 shows the demultiplexing properties of a 400-channel 25-GHz-spacing AWG. Crosstalk levels of about -30 dB have been achieved. Super high Δ waveguides with a refractive index core cladding contrast of 1.5% were used in the 400-channel 25-GHz AWG to minimize the area of the array waveguide region. Fig. 6 shows the demultiplexing properties of a 32-channel AWG with a very narrow channel spacing of 10 GHz without using a post process for phase error (nonuniformity in the optical path-length difference $n_c\Delta L$) compensation. Here, a high Δ waveguide with a refractive index difference of 0.75% was used. An adjacent channel crosstalk of about -30 dB has been achieved even in the 10-GHz-spacing AWG. Postfabrication phase error compensation techniques can further improve the crosstalk of AWGs.

C. Crosstalk and Dispersion Characteristics of AWGs

1) Crosstalk of AWG: The crosstalk of an AWG is mainly attributed to the phase (optical path-length) fluctuation in the arrayed waveguides [10]. If there were no phase (or amplitude) errors, we could obtain about a -60-dB level in this example ($\delta n = 0$ in Fig. 7). The reason why we could not achieve such a low crosstalk level is that the envelope of the electric field at the second slab interface does not have a smooth Gaussian shape. Phase errors are caused by effective index nonuniformities in the arrayed waveguide region; that is, refractive index fluctuations and core width and thickness nonuniformities. Fig. 7 shows the demultiplexing properties of AWGs having a sinusoidal phase fluctuation of $\delta n = 1 \times 10^{-6}$ with $\Lambda = N/10$ for three kinds of AWGs with 100-, 50-, and 25-GHz channel spacings, respectively. The spatial sinusoidal phase fluctuation is assumed to be expressed by

$$\tilde{n}_c(\ell) = n_c(\ell) + \delta n(s) \cdot \sin\left[\ell\frac{\pi}{\Lambda(s)}\right] \tag{12}$$

where ℓ is an integer from 1 to N and denotes the array number and order of spatial frequency in fluctuation, $n_c(\ell)$
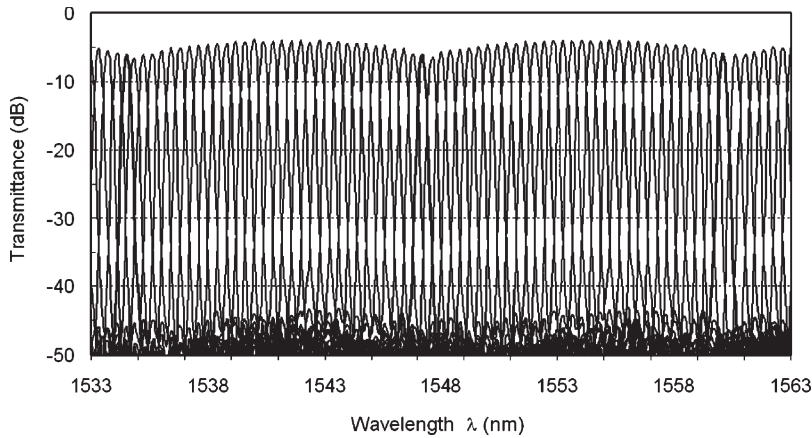
Fig. 4.   Demultiplexing properties of 32-channel 50-GHz-spacing AWG over four diffraction orders.
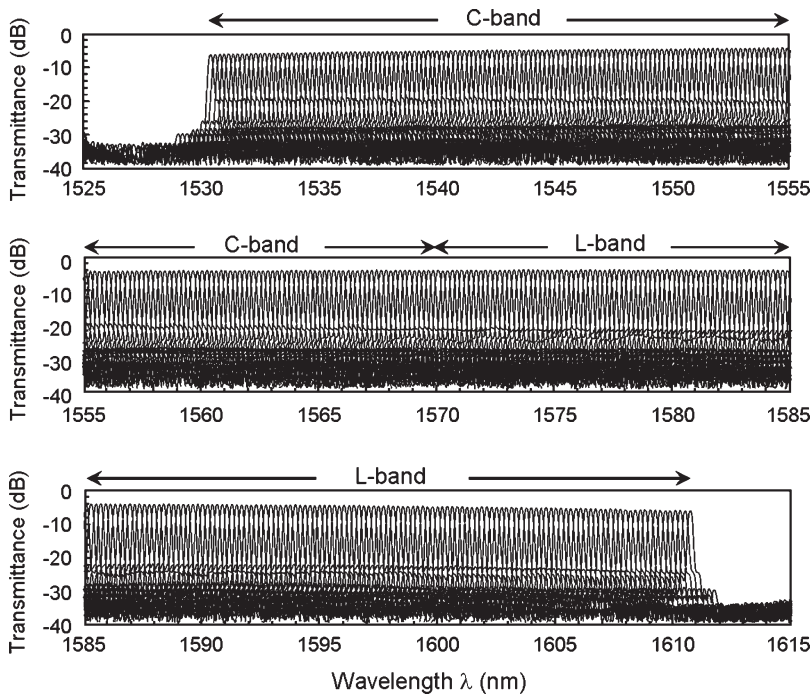

Fig. 5.   Demultiplexing properties of 400-channel 25-GHz-spacing AWG.
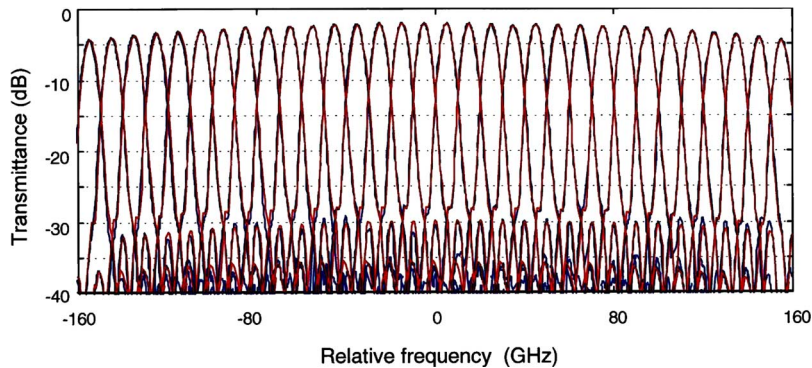

Fig. 6.   Demultiplexing properties of 32-channel 10-GHz-spacing AWG.

is the ideal effective index distribution, δn is an amplitude of fluctuation, and Λ is a half period of index fluctuation. It is known empirically that crosstalk degrades by about 5 dB when the channel spacing is cut in half. It is also known that crosstalk degrades by about 10 dB when δn becomes about 3.2 $(= \sqrt{10})$ times larger. For the phase fluctuations, the sidelobe level strongly depends on the channel spacing.
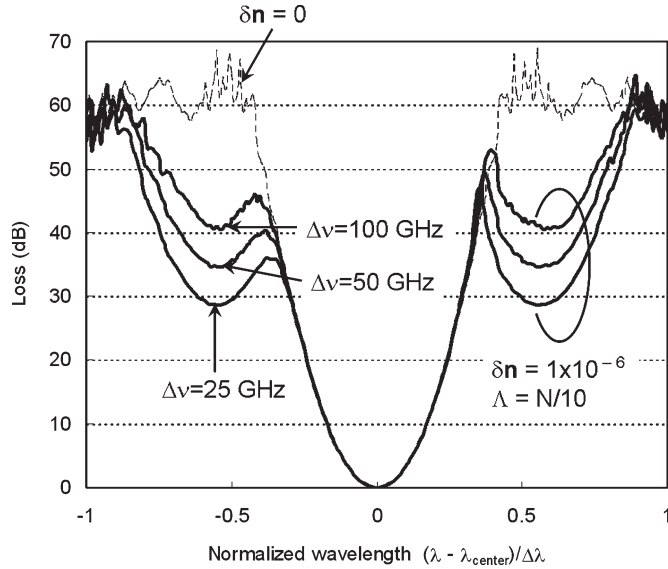
Fig. 7. Theoretical demultiplexing properties of AWGs having sinusoidal phase fluctuation of $\delta n = 1 \times 10^{-6}$ with $\Lambda = N/10$ for three kinds of AWGs with 100-, 50-, and 25-GHz channel spacing.

2) Dispersion of AWG: Phase errors cause not only crosstalk but also chromatic dispersion in the AWG itself [11]. Fig. 8 shows the theoretical dispersion properties of 64-channel 100-GHz-spacing to 64-channel 25-GHz-spacing AWGs having spatially sinusoidal phase fluctuations given by (12). It is shown that a spatially low-frequency phase fluctuation (small s) causes dispersion inside the passband of the AWG. Here, dispersion values are fixed to be -15 ps/nm in Fig. 8(a)–(c) and $+15$ ps/nm in Fig. 8(d)–(f). Then, the index fluctuation δn that generates the specified dispersion is calculated. It is known empirically from several calculations, including Fig. 8, that the dependence of dispersion σ on index fluctuation δn and channel spacing $\Delta\nu$ is approximately obtained as $\sigma \propto \delta n/\Delta\nu^3$. Since σ is inversely proportional to $\Delta\nu^3$, the dispersion of an AWG with a narrow channel spacing is much more susceptible to phase errors.

D. Flat Spectral Response AWGs

Since the rate of displacement of the focal position x with respect to the wavelength λ is almost constant (5), the transmission loss of a Gaussian AWG monotonically increases around the center wavelength of each channel. This places tight restrictions on the wavelength tolerance of lasers and requires accurate temperature control for the AWGs. Moreover, since optical signals may be transmitted through several filters in WDM ring/bus networks, the cumulative passband width of each channel becomes much narrower than that of a single-stage AWG filter. One solution is to make the Gaussian AWG passband very wide compared to the channel spacing, as discussed in Section II-F1. This may be acceptable when the AWG is used as a multiplexer. However, it is not acceptable when the AWG is used as a demultiplexer because of the high crosstalk due to overlapping adjacent passbands. Therefore, flattened and broadened spectral responses with steep spectral

skirts (i.e., a rectangular passband) are often required for AWG demultiplexers.

Several approaches have been proposed to flatten the passbands of AWGs [12]–[17]. One is to create a flat electric field distribution at the input waveguide. Since the AWG is an imaging device, the flat electric field is reproduced at the output plane. The overlap integral of a flat field with a Gaussian local normal mode gives a flat spectral response. Parabolic waveguide horns [13] or 1×2 multimode interference couplers [14] are used to create a flat electric field distribution at the input waveguide. The second method is to engineer the waveguide array design to create a flattened electric field at the output plane. In this case, the input field is a normal Gaussian distribution. There are mainly two techniques to achieve this second method. One is to make a sinc-like electric field envelope in the array waveguides [12]. Since the focused electric field profile is a Fourier-transformed image of the electric field in the array waveguides, we can generate a flattened field distribution at the output plane. The other is to make two focal spots at the output plane [15]. Here, the light-focusing direction of the array waveguide is alternately changed to two separate focal positions. In this case, the flattened field profile consists of two Gaussian beams.

There are some other flattening techniques employing somewhat sophisticated operational principles [16], [17]. In these techniques, the input position of the beam moves synchronously with the wavelength change of the signal, and they are discussed in Section II-E. Then, the output beam lies in a fixed position independent of wavelength within one channel span.

1) Parabola-Type AWG: The inset in Fig. 9 shows an enlarged view of a parabola-shaped input waveguide. The width of the parabolic horn along the propagation direction z is given by [18]

$$W(z) = \sqrt{2\alpha\lambda_g z + (2a)^2} \qquad (13)$$

where α is a constant less than unity, λ_g is the wavelength in the guide ($\lambda_g = \lambda/n_c$), and $2a$ is the core width of the channel waveguide. At the proper horn length $z = \ell$ less than the collimator length, a slightly double-peaked intensity distribution can be obtained, as shown in Fig. 9. A broadened and sharp-falling optical intensity profile is obtainable by the parabolic waveguide horn, which is quite advantageous for achieving a wide passband without deteriorating the nearest-neighbor crosstalk characteristics. The broadened and double-peaked field is imaged onto the entrance of an output waveguide having a normal core width. The overlap integral of the focused field with the local normal mode of the output waveguide gives a flattened spectral response for the AWG. Fig. 10 shows the demultiplexing properties of a 32-channel 100-GHz-spacing AWG having parabolic horns with $W = 26.1 \ \mu$m and $\ell = 270 \ \mu$m.

In a parabola-type flat AWG, the double-peaked electric field distribution is created by the interference of the fundamental mode and the second-order mode. Generally, the phase retardations of the fundamental mode and second-order mode are different. Therefore, the total phase at the end of the parabolic waveguide horn is not a uniform phase distribution. A nonuniform phase distribution in the parabola input waveguide
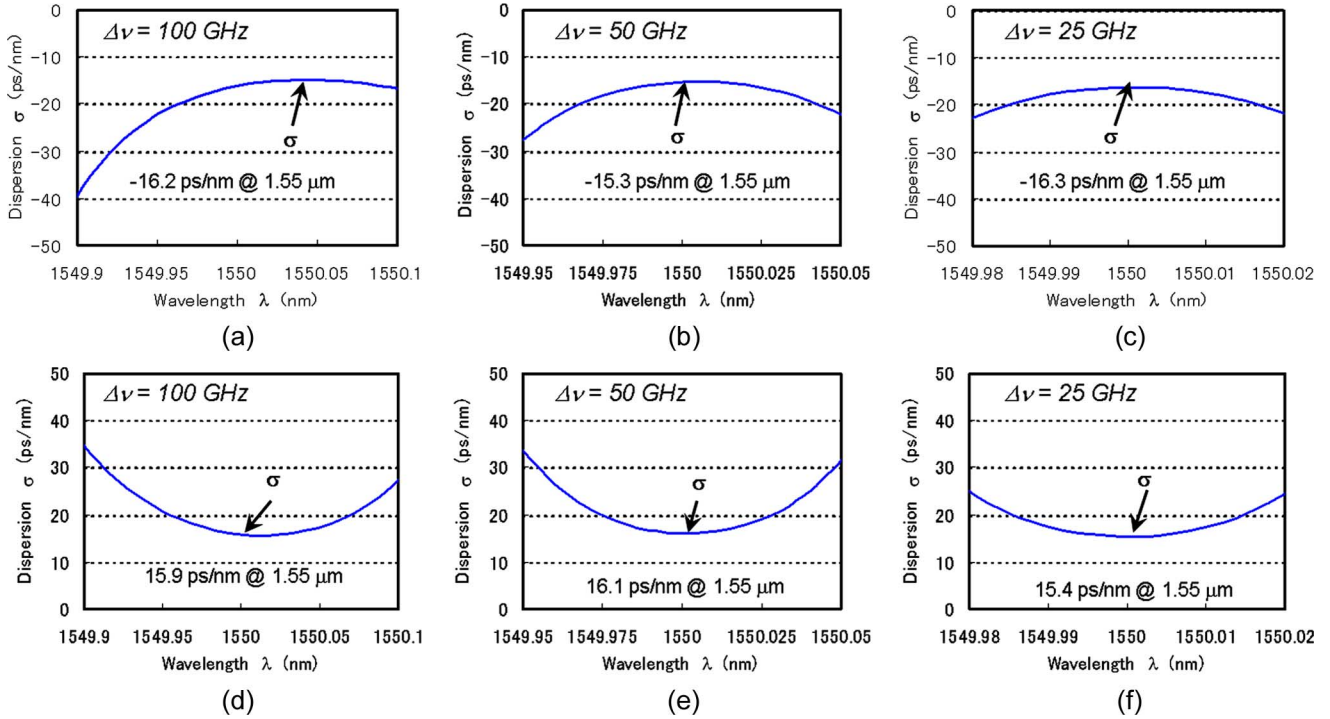
Fig. 8.   Theoretical dispersion characteristics of three kinds of AWGs with 100-, 50-, and 25-GHz channel spacing for various kinds of index fluctuation δn.
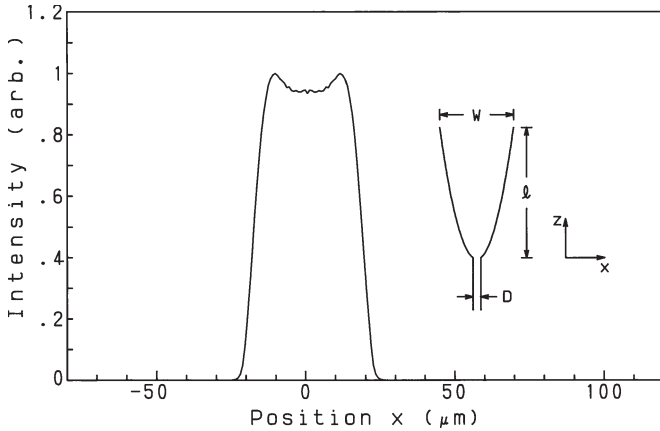

Fig. 9.   Intensity profile calculated by the BPM in the parabolic input waveguide. Inset shows the schematic configuration of parabolic waveguide.
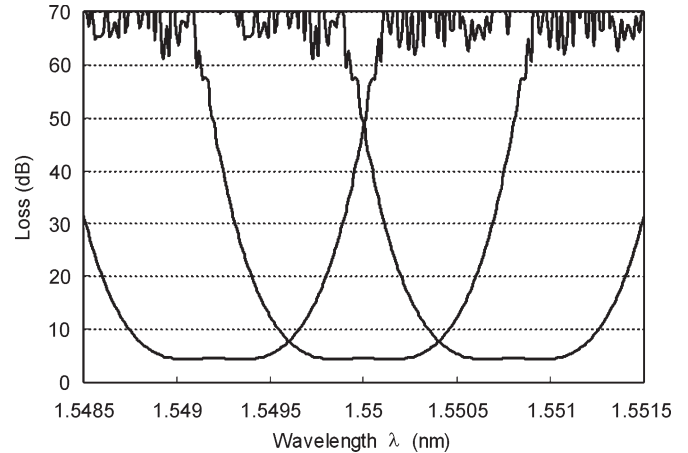

Fig. 10.   Demultiplexing properties of 32-channel 100-GHz-spacing AWG having parabolic horns with $W = 26.1$ μm and $\ell = 270$ μm.

causes nonuniformity of phase in the array waveguides. It is known that such a nonuniform phase is similar to effective index fluctuations in the array waveguides and thus can cause chromatic dispersion as described in the previous section. Fig. 11 shows the theoretical and experimental dispersion characteristics of a 32-channel 100-GHz parabola-type flat AWG.

Phase retardations between the fundamental and the second-order modes at the end of the parabolic waveguide horn can be adjusted by adding a straight multimode waveguide, as shown in Fig. 12 [19]. At the proper multimode waveguide length, phase retardations of the fundamental and second-order modes are almost equalized. The total phase distribution becomes uniform while the double-peaked electric field distribution is maintained. The theoretical and experimental dispersion characteristics of the 32-channel 100-GHz parabola-type flat AWG with $W = 26.1$ μm, $\ell = 270$ μm, and $L_{multi} = 85$ μm

are shown in Fig. 13. Chromatic dispersion has been reduced to a negligible value.

E. AWGs With Periodic Stationary Imaging

1) Achieving Multiple Zero-Loss Maxima: As discussed in the previous section, when optical filters, such as a wavelength demultiplexer, are used in WDM fiber-optic communication systems, it is often desirable that the passband magnitude have a rectangular shape and the passband phase change linearly with optical frequency. A rectangular shape means that the passband magnitude is flat on top and falls off steeply on both sides. Such a filter distorts signals passing through it very little (provided the passband is wide enough) and can be cascaded (many such filters encountered in series) with low net signal
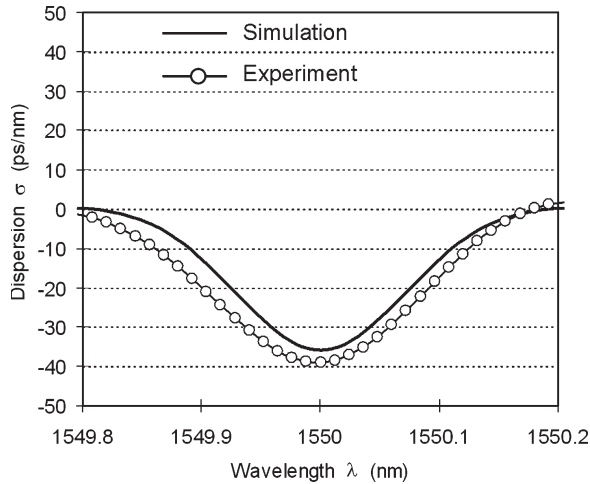
Fig. 11. Theoretical and experimental dispersion characteristics of a 32-channel 100-GHz parabola-type flat AWG.
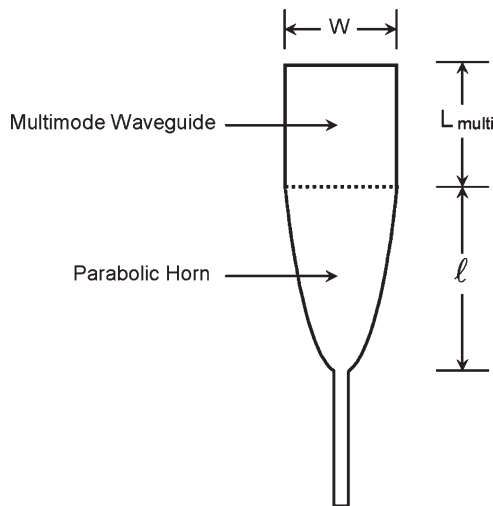

Fig. 12. Parabolic waveguide having a straight multimode waveguide.

Fig. 13. Theoretical and experimental dispersion characteristics of 32-channel 100-GHz parabola-type flat AWG with $W = 26.1$ μm, $\ell = 270$ μm, and $L_{\text{multi}} = 85$ μm.

distortion. A linear phase means that the passband has zero chromatic dispersion.

How rectangular a passband is can be quantified by the number of maxima in the passband. For instance, a standard AWG has a Gaussian-shaped passband, which has one maximum in the passband. Such a passband is far from being rectangular. However, if we have two maxima in the passband, then already the passband starts to look rectangular. The maxima in the passband can be at different frequencies or at the same frequency. When many of the same optical filter are placed in series, the net cascaded passband is simply a stretching of the scale of the passband if it is plotted in decibels (in actuality, small variation from filter to filter complicates this). For example, the 0.3-dB down point on the passband becomes the 3-dB down point after ten cascades. The passband shape is stretched downward around the maxima. Thus, the more maxima (provided the maxima are at the same magnitude), the more the passband is "held open."

As shown in Section II-D, one way to add more maxima to an AWG passband is through image mismatching, i.e., the image
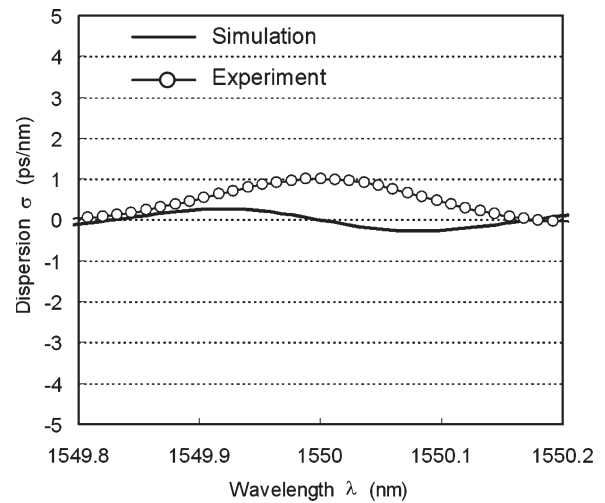
from the input waveguide does not match the image that an output waveguide would make. Such a method is compact and robust. However, image mismatching adds optical loss. This section addresses adding maxima without adding loss.

Any optical filter can be represented in the time domain by its impulse response. For the discussion here, we will limit ourselves to optical filters that are periodic, with a free spectral range (FSR) equal to Δf. Thus, the time-domain impulses are spaced by $1/\Delta f$. If a filter has one zero-loss maximum per FSR, then the sum of the magnitudes of the impulses (in optical amplitude, not power) is equal to a zero-loss maximum in the spectrum. If a filter has more than one zero-loss maximum per FSR, then this sum must be greater than unity. Otherwise, all the impulses must be in phase to achieve a zero-loss maximum in the spectrum, and this can happen only once per FSR.

The impulse response of an optical filter is measured by sending an impulse into the filter and recording the impulses that exit the filter. Each possible path through the filter generates an impulse. Not every path generates an independent impulse since multiple paths may have the same length. For a periodic filter, all path lengths are an integer multiple of a unit length.

If the filter consists of a $1 \times N$ coupler, N arms, and an $N \times 1$ coupler, i.e., an MZI (if $N = 2$) or an AWG (if $N > 2$), then the sum of the impulse amplitude magnitudes cannot be greater than one; otherwise, power conservation is violated. This is because each impulse is generated by one arm, so it is possible that at some frequency all impulses are in phase. Thus, it is impossible for an AWG to have more than one zero-loss maximum per passband per FSR, regardless of what arm length distribution, input mode shape, or output mode shape is chosen. Furthermore, concatenating such filters, which are filters interconnected by a single mode, cannot create a net filter with an impulse response magnitude sum that is greater than unity because the convolution of two impulse trains each with a magnitude sum that is not greater than unity cannot have a magnitude sum that is greater than unity.
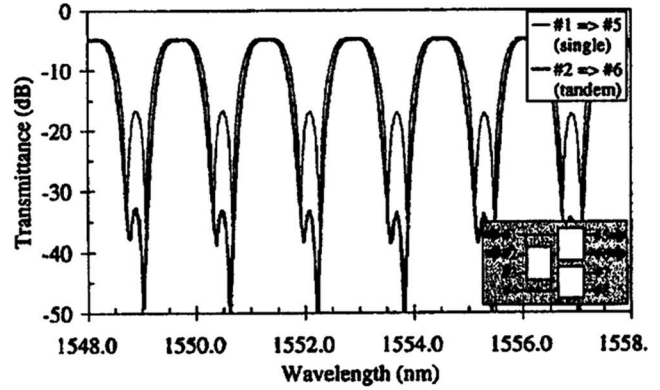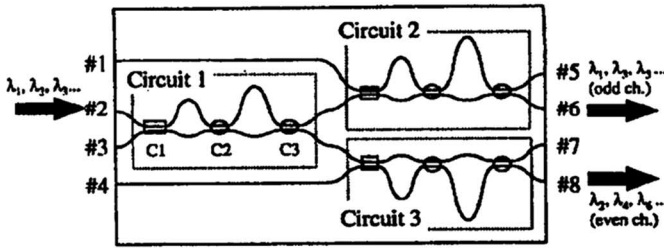
Fig. 14. Fourier-filter-based interleaver and concept for achieving zero dispersion with 2×2 filters. As one can see, the port-pair combination in the left stage is complementary to the port-pair combination in the right stage.

Thus, we have proven the following theorem.

Theorem 1: It is impossible to generate more than one zero-loss maximum per FSR if the filter contains only $1 \times N$ (or, equivalently, $N \times 1$) couplers.

Then, how can one generate an impulse response with a magnitude sum greater than unity? The answer is to use at least one $M \times N$ coupler, where $M, N > 1$. Such a coupler can generate "extra" impulses such that one waveguide can be responsible for generating more than one impulse.

A good example of this is the Fourier filter interleaver, shown in Fig. 14. This filter can theoretically have zero loss at two wavelengths per FSR, because it contains one 2×2 coupler. Such a filter has a chromatic dispersion. However, this can be overcome by cascading two identical filters in series, where one connects one port of the first filter to the complementary port of the second filter [20]. This works because in a 2×2 filter, the amplitude transmissivity from one input port to one output port is equal to the complex conjugate of the amplitude transmissivity between the other input port to the other output port.

2) AWG With Two-Arm-Interferometer Input: Using the theorem we just proved, we realize that a conventional AWG can have only one zero-loss maximum per FSR. In this section, we would like to create an AWG with two zero-loss maxima per FSR. To do this, we will have to connect the device input to more than one input to the first AWG star coupler (or equivalently connect the device output to more than one output from the second AWG star coupler).

To figure out what to connect between the device input and the two star coupler inputs, note that the problem with a conventional AWG is that the image in the second star coupler is always moving as the wavelength increases. To create two zero-loss maxima per FSR, we need to have the image focus on the output waveguide in the second star coupler twice per FSR. To do this, we need to move the image in the first star coupler as the wavelength changes. We can accomplish this by having a length-imbalanced MZI connected to the two inputs of the first star coupler, where light moves from one input to the second as the wavelength changes such that both images focus on the same output waveguide [17], [21]. If we then match the FSR of the MZI to the channel spacing of the AWG, then one MZI can create dual zero-loss maxima for all channels.
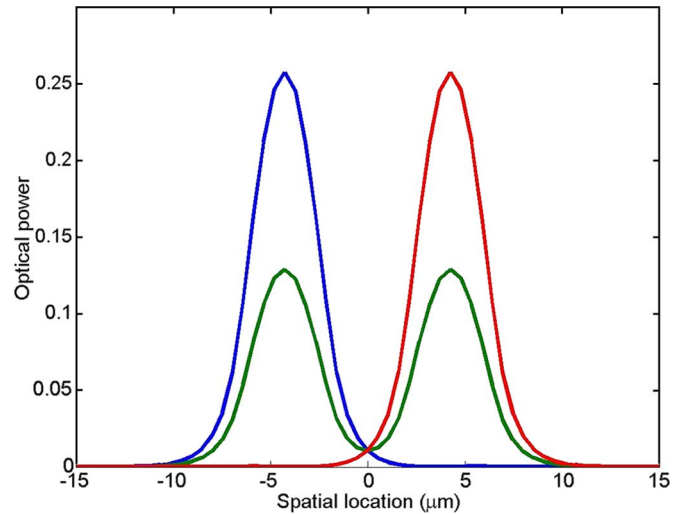

Fig. 15. Change in optical field at end of a length-imbalanced MZI with a directional 2×2 coupler as the optical frequency is changed.

Fig. 15 shows a plot of the optical power from the MZI at the MZI–star coupler junction as the wavelength changes. The light switches from one output to the other. In between these states, the light is partly in one output or the other. One can view the "center of mass" of the optical distribution as moving continuously between the two states. Since this is imaged by the AWG onto the output waveguide, one can view the MZI as making the center of mass of the image stationary on the output waveguide. This is what creates the desired low-loss flat-top passband.

Two possible ways of laying out the MZI-AWG are shown in Fig. 16. Fig. 16(a) shows the MZI and AWG having the same sign of "curvature." This is necessary for the synchronization of the MZI and AWG at their interconnection point. Fig. 16(b) shows a switching of the sign of curvature. This is possible by having a sort of waveguide crossing in the MZI, that is effected by using a 100/0 coupler. It is found that a relative phase shift of 180° between the waveguides connecting the 100/0 coupler to the 50/50 coupler minimizes the performance sensitivity to wavelength, fabrication, and polarization changes.

Fig. 17 shows an actual waveguide layout and the resulting measured transmissivity. Theoretically, the chromatic
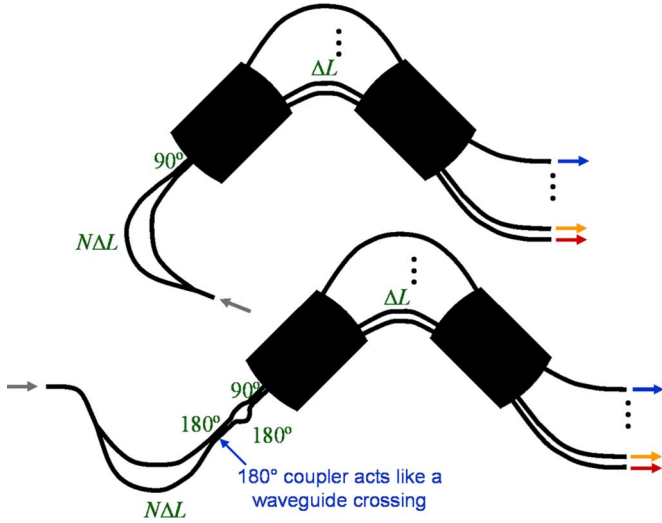
Fig. 16. Possible layouts for a rectangular passband demultiplexer consisting of an MZI directly connected to an AWG.

dispersion in the passband is zero. However, if the 50/50 coupler has a splitting ratio error, then the device will exhibit dispersion. This can be understood by following a signal passing from right to left through the device. Suppose the 50/50 coupler is too weak. Then, when the signal from the AWG is imaged onto the upper waveguide of the 50/50 coupler, which is the short-wavelength side of the passband, then instead of the signal being divided evenly between the two MZI arms, more light will be coupled to the longer MZI arm. The effective path length through an interferometer is equal to the average of the path lengths weighted by the optical power in each arm. Thus, the total path length through the device will be longer on the shorter-wavelength side of the passband. It will be vice-versa for the longer wavelength portion. Thus, the passband will exhibit negative dispersion.

3) AWG With Three-Arm Interferometer Input: We just showed how to create a passband with two zero-loss maxima by connecting a two-arm interferometer to an AWG. One can extend this principle by using a larger number of arms in the input interferometer. However, many difficult technical challenges arise once the number of arms is greater than two. Here, we address them for an arm number of three [22], [23].

The main challenge with going from two arms to three arms is the directional coupler that connects to the AWG. As we will show, a three-arm directional coupler is not trivial, and it is has an undesirable phase relationship between the outputs. One might think why not turn the input interferometer into a small AWG and use a star coupler? However, a star coupler with a low port count ($\sim< 8$) has a very low efficiency, undoing our intent of making a low-loss flat-top passband. A star coupler with a low port count has a low efficiency because the waveguides converge too quickly to convert the plane waves of the free-space region to only first-order Bloch modes of the waveguide array.

The problem with the three-waveguide directional coupler is that the difference of the phase between adjacent output waveguides from the coupler when illuminating one input waveguide of the coupler is always an integer multiple of 90°, whereas we would like it to be an integer multiple of 120°. We

would like it to be 120° because this is the phase difference encountered in an ideal star coupler. The phase between port m_1 on one side and m_2 on the other side of an ideal $M \times M$ star coupler is

$$\phi = \frac{2\pi}{M} \left(m_1 - \frac{M+1}{2} \right) \left(m_2 - \frac{M+1}{2} \right). \quad (14)$$

For $M = 3$, one can see that this gives either 0° or 120° phase difference. The 90° phase difference encountered in the directional coupler means that the three passbands per FSR from the input interferometer are unequally spaced in frequency, and the resulting interferometer-plus-AWG device exhibits mostly a two zero-loss maxima passband. However, using a multisection three-waveguide directional coupler, one can achieve the desired phase difference and achieve a three zero-loss maxima passband. The design and results are shown in Fig. 18.

If we wish to use more than three arms and not use a star coupler for the second coupler of the input interferometer, then we have a difficult problem with the design of the input interferometer. As shown in [24], if one makes a demultiplexer using a multimode interference coupler (and likewise with a directional coupler), the arm lengths no longer follow a linear progression in path length when the arm number is greater than three.

F. AWGs With High Spectral Sampling

Suppose we have a conventional AWG with one input and N outputs, and we launch a signal into the input. The N outputs take discrete "samples" of the spectrum of the input signal, spaced in spectrum by a certain amount and "filtered" by a certain "bandwidth" [25]. This is analogous to sampling in the time domain, in which a waveform is sampled by discrete-time sample points spaced in time by a certain amount and filtered by a certain "bandwidth."

1) Sampling Theorem: For the time-domain case, if the spectrum is zero for frequency $|f| > f_B/2$, and the signal is sampled in time by spacing T, then we can define a sampling coefficient

$$s = \frac{1}{Tf_B}. \quad (15)$$

The sampling theorem states that if $s \geq 1$, then the signal is uniquely determined by its samples.

We can derive a similar relation for the AWG in the spectral domain. The field along one edge of a star coupler is approximately the spatial spectrum (i.e., Fourier transform) of the field along the other edge. The output waveguides of the AWG are thus sampling the spatial spectrum of the field from the grating arms. If we make this field zero outside of a spatial width w, and if the output waveguides are spaced closely enough, then the samples in the output waveguides can uniquely determine the field along the grating arm edge of the output star coupler in the AWG. This field is determined by the input signal spectrum. Thus, we can uniquely determine the input spectrum by these discrete samples. To make the field zero outside of width w, we can simply use a limited number of grating arms in the AWG. $w = Ma$, where M is the number of grating
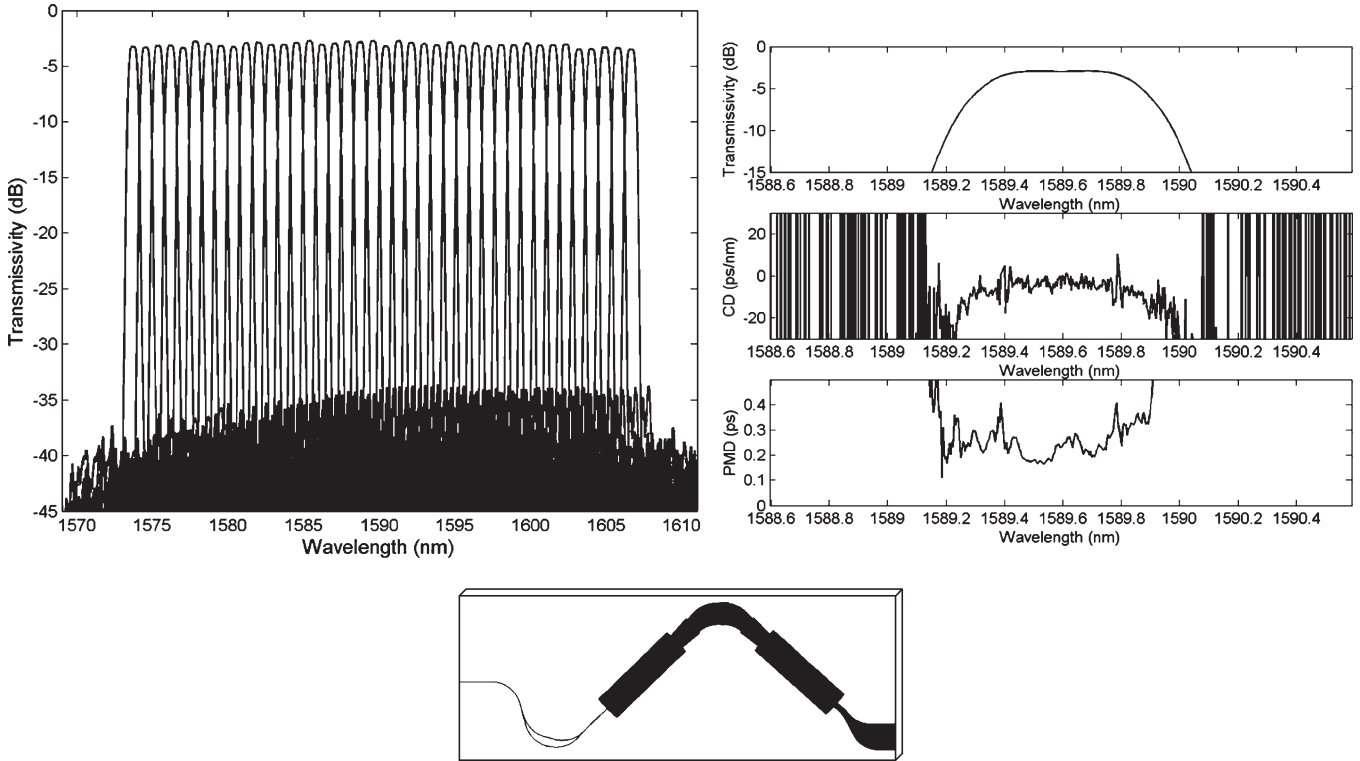
Fig. 17. Waveguide layout and measured results from a demultiplexer consisting of an MZI directly connected to an AWG.
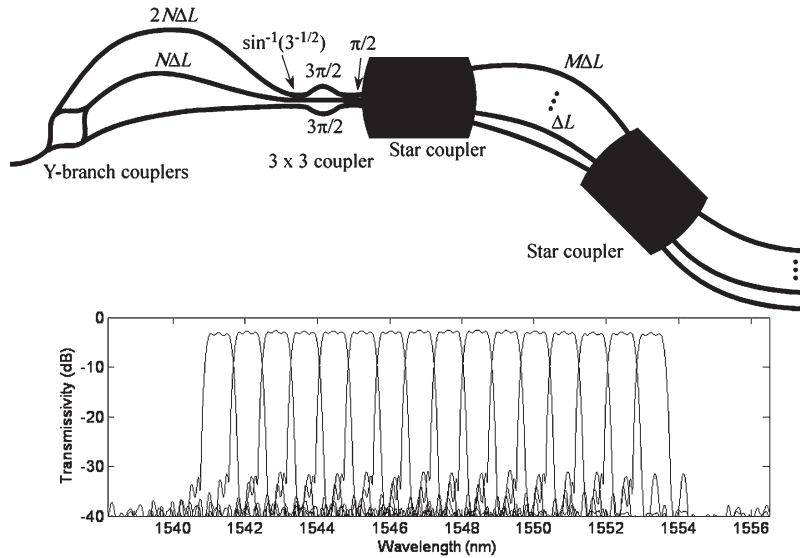

Fig. 18. Sixteen-channel demultiplexer consisting of a three-arm interferometer directly connected to an AWG.

arms, and a is the grating arm pitch at the connection to the output star coupler. Note that the star coupler can still have dummy waveguides outside of width w, to which the field can couple, because the dummy waveguides are necessary for the star coupler to perform an accurate Fourier transform.

If the output waveguides have pitch b at their connection to the output star coupler, then the sampling coefficient is

$$ s = \frac{R\lambda}{Mab} \qquad (16) $$

R is the star coupler radius (i.e., length), and λ is the wavelength in the slab (i.e., not the free-space wavelength). Thus, if $s \geq 1$,

the information in the output waveguides is sufficient to uniquely determine the AWG input signal. Note that because there are a finite number of output waveguides, the signal spectrum must be bandlimited for this to be true. It is analogous to the time-domain case, in which the signal must be limited in its time extent because only a finite number of time sampling points can be recorded.

Interestingly, when $s = 1$, the output star coupler is an $M \times M$ star coupler, although it is possible that less than M output waveguides are actually used.

One use for an AWG with high sampling is as a multiplexer with passbands as wide as possible and no concern for crosstalk
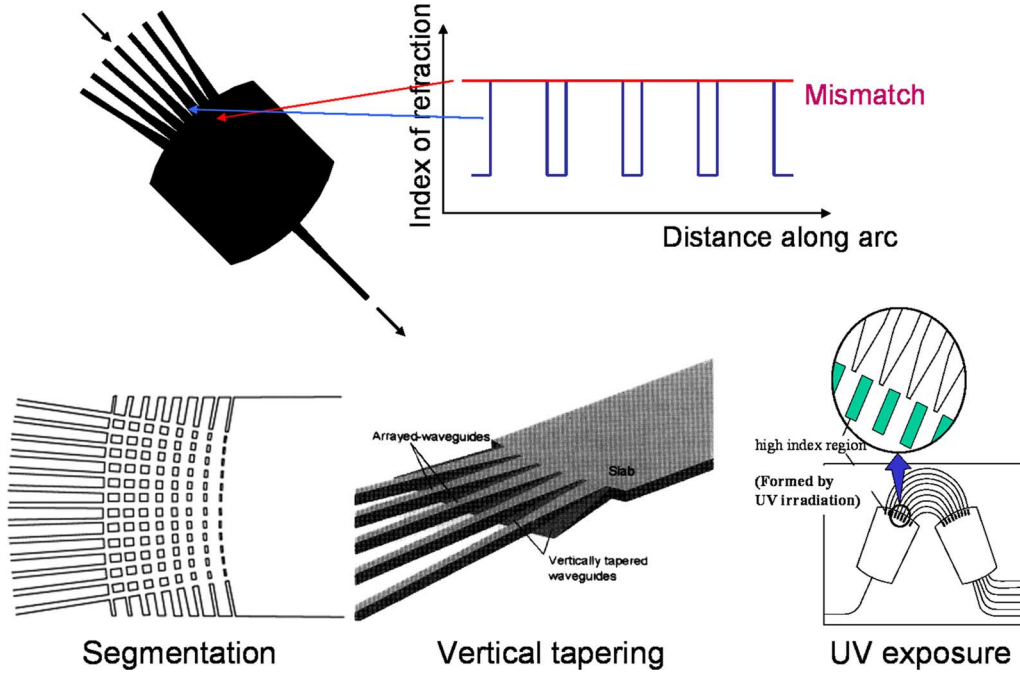
Fig. 19. (Top) Mismatch in refractive index distribution at the slab-to-array transition in a star coupler, which is a significant source of insertion loss in AWGs. (Bottom) Various demonstrated schemes for reducing this loss.

level. Other uses include making a dynamic gain equalization filter (DGEF) and a band de/multiplexer, which is described later in this section.

2) Aberrations: A conventional Gaussian passband AWG demultiplexer has $s \approx 0.5$. As s is increased toward 1 and beyond, a significant problem in the AWG usually develops: the output waveguides become so close that there is significant mutual coupling between them. If left uncorrected, this results in aberrations that give high loss and large passband shoulders. To mitigate the mutual coupling, one could increase b. However, this results in a longer R [see (16)] and a larger device size. A better solution is to move the aiming point of the grating waveguides into the output waveguides and then slightly modify the grating arm path lengths [26].

To calculate how much to adjust the grating arm lengths, one must calculate the transmissivity from each grating waveguide through the second star coupler to each output waveguide. When there is mutual coupling between the waveguides, a useful tool is BPM. Many types of BPM exist, such as Fourier transform BPM (FT-BPM) and finite-difference BPM (FD-BPM). FT-BPM can handle wide angles but is slow and cannot handle large index steps. FD-BPM is much faster and can handle large index steps but cannot handle wide angles. There is another type called sinc BPM [27], which is based on FT-BPM but stays in the angular spectrum domain. It is fast and accurate for periodic waveguide arrays, such as encountered in star couplers.

To calculate the transmissivities mentioned earlier, we first calculate the waveguide mode of an uncoupled grating waveguide. Then, we use BPM to propagate it until it reaches the star coupler boundary. Call this field u_1. Then, we calculate the waveguide mode in an uncoupled output waveguide and use BPM to propagate it until it reaches the star coupler boundary. Call this field u_2. The transmissivity although the second star

coupler in an AWG from a grating waveguide at angle θ_1 to an output waveguide at angle θ_2 is

$$t(\theta_1, \theta_2) = \frac{\int_{-\infty}^{\infty} u_1^{\mathrm{prop}}(x) u_2(x) \exp\left[jkx(\theta_2 - \angle AB)\right] dx}{\sqrt{\int_{-\infty}^{\infty} |u_1(x)|^2 dx \int_{-\infty}^{\infty} |u_2(x)|^2 dx}} \tag{17}$$

$$AB = R(e^{-j\theta_1} - 1 + e^{j\theta_2}) \tag{18}$$

$$u_1^{\mathrm{prop}}(x) = F^{-1}\Big\{ F\left\{ u_1(x) \exp\left[jkx(\theta_1 - \angle AB)\right]\right\} \\ \times \exp\left(j\sqrt{k^2 - k_x^2}|AB| \right) \Big\} \tag{19}$$

$$F\{u(x)\} = \int_{-\infty}^{\infty} u(x) e^{jxk_x} dx. \tag{20}$$

In general, when designing a star coupler with mutual coupling between waveguides, it is best to aim for making u_1 and u_2 such that the power coupled to each of the two adjacent waveguides is ~4 dB less than the power in the launched waveguide. Increasing the mutual coupling beyond this tends to make the device too sensitive to fabrication details.

Just as segmentation [28], vertical tapering [29], or selective UV exposure [30] (see Fig. 19) improve the AWG grating efficiency, these techniques can also improve the coupling efficiency to highly sampled output waveguides. They work by reducing the abruptness of the transition from the waveguide array to the slab region. Segmentation is the easiest to implement since it does not require any extra fabrication steps. In segmentation, one simply adds sections (15 is a typical number) perpendicular to the waveguides. The section center-to-center spacing is constant, but their widths gradually decrease as their distance from the slab increases.

3) DGEF: In Section II-E1, we proved that we need $N \times M$ couplers, where $N, M > 2$ to create a passband with more
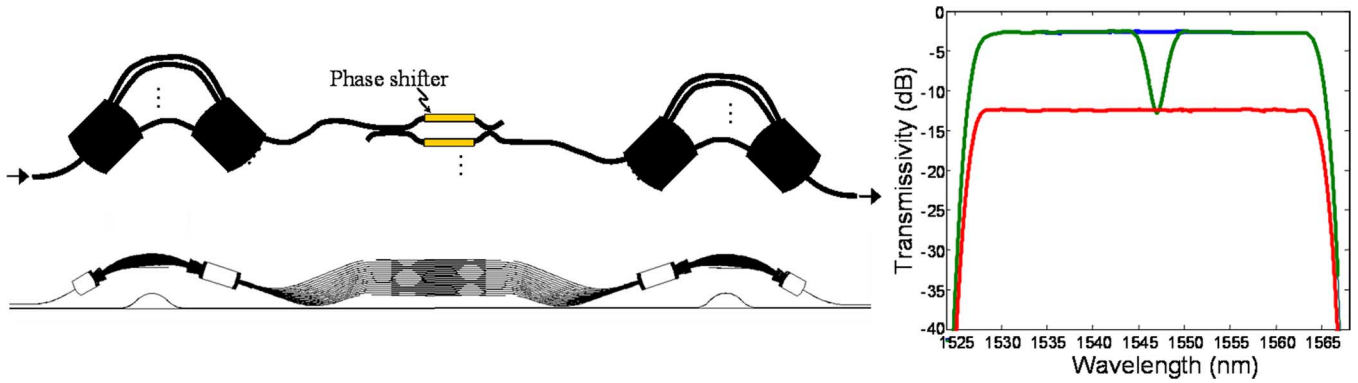
Fig. 20.   DGEF consisting of two AWGs connected by an AWL. Upper left is the concept, lower left is the actual waveguide layout (has 16 waveguides in the AWL), and the right is the measured response, fiber-to-fiber.
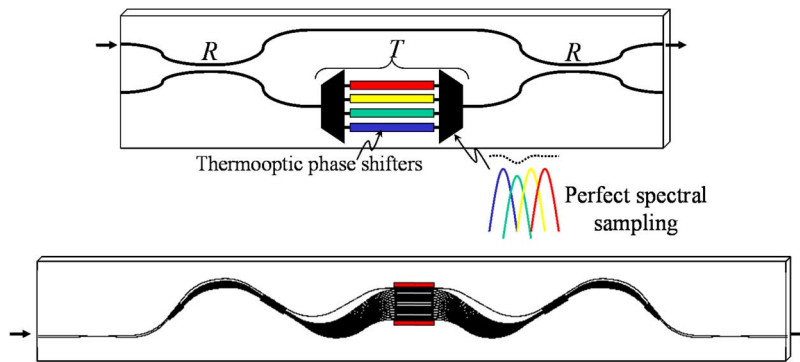

Fig. 21.   Lower loss DGEF using a large interferometer.

than one zero-loss maximum. In Sections II-E2 and 3, we then showed how to make a two-maxima passband and a three-maxima passband by connecting two-arm and three-arm interferometers, respectively, directly to an AWG. Here, we connect one AWG to another AWG via an arrayed waveguide lens (AWL) to create a passband with numerous zero-loss maxima. By inserting either phase shifters or VOAs into the AWL arms, we create a dynamic filter that can control the channel powers in a WDM link, which is often called DGEF [31].

An AWL is an AWG with a grating order of zero, i.e., the path lengths of all the arms in the "grating" are equal. In order to lay out such a structure without waveguides running into each other, the conventional "U"-shaped structure of an AWG cannot be used. Instead, it is best to use a "W"-shaped structure.

We would like the DGEF to be able to pass all the WDM channels in a given spectral region without any distortion. In order to do this, the AWL ports must perfectly or oversample the spectra from the AWGs, i.e., $s \geq 1$ for all AWL ports and all λ in the spectral region of interest.

A layout for a DGEF is shown in Fig. 20. There is an MZI with thermo-optic (TO) phase shifters in each arm. Each MZI must be driven in a push–pull fashion to maintain a constant phase difference between adjacent AWL arms. Using push–pull also reduces the polarization dependence due to the fact that it reduces the maximum required phase shift, and a typical silica TO phase shifter shifts TM-polarized light 4% more efficiently than TE-polarized light. Push–pull also reduces the worst-case power consumption and keeps the total heat dissipation constant [31]. A measured spectral response through the DGEF

is shown in Fig. 20(right) when all VOAs are set for minimum attenuation and when one VOA is set for increased attenuation. One can see that the spectral response is smooth and ripple free despite the fact that the spectrum is broken into discrete sections by the AWGs.

There is another DGEF arrangement that has a lower insertion loss, which is shown in Fig. 21. It consists of a large interferometer with one arm containing an AWG–AWL–AWG series [32]. In this DGEF, each AWL arm contains just a phase shifter rather than an MZI. The couplers of the interferometer do not have to have a 50/50 coupling ratio. The overall insertion loss is lower than the insertion loss of the AWG–AWL–AWG series because only a portion of the light passes through the AWG–AWL–AWG series. The main drawback to this design is that because of the large interferometer with very different elements in each interferometer arm, it is difficult to make it insensitive to the environment and the input light polarization. One way to solve the polarization-dependence difficulty is to use polarization diversity.

4) Band Multiplexer: The DGEF can be a band filter, i.e., a filter with a very wide passband and very steep sidewalls. With a small modification, one can change it into a band de/multiplexer (we will call it just a multiplexer from here on) [33]. The concept is shown in Fig. 22. In this case, the AWL is split into groups at one end. Because each group enters the right-hand AWG at a different location, the spectral portions carried by each group are sent to different outputs. Note that in this design, it is not necessary that the AWL arm path lengths be the same from group to group.
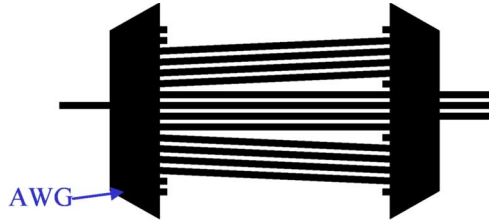
Fig. 22. Concept of band de/multiplexer using AWGs.

It is important to note that this band multiplexer does not exhibit any chromatic dispersion. This is because all path lengths are the same for all wavelengths (provided the aberrations have been compensated for). This is possible because AWG filters are nonminimum phase filters [34]. Thus, AWGs need not obey the Kramers–Kronig relations and can have rectangular-shaped passbands and a linear phase simultaneously. This is unlike conventional band filters that are made from thin-film technology. Those band filters are made from a series of resonances and are infinite impulse response (IIR) filters. In transmission, thin-film filters are minimum phase filters and thus obey the Kramers–Kronig relations. These filters have significant dispersion at sharp passband corners, resulting in signal distortion.

A waveguide layout and measured results from a five-band eight-skip-zero multiplexer are shown in Fig. 23 [35]. A-skip-B means that each band carries A number of channels (typically on a 100-GHz grid), and there are dead zones of B channels between them. As expected, chromatic dispersion is negligible, even at the passband corners.

There is a type of WDM called coarse WDM (CWDM) that has a 20-nm channel spacing. The channel spacing is so wide because it is designed for uncontrolled laser transmitters. The passbands for CWDM typically must be wide and flat with a bandwidth greater than 14 nm. The band multiplexer is a good way to make a CWDM de/multiplexer. Fig. 24 shows a waveguide layout for an eight-channel CWDM multiplexer and the measured response [36]. Because the channel spacing is so wide, the AWG grating orders are very small, and having unequal path lengths in the AWL adds a negligible amount of chromatic dispersion (allowing one to use a "U" shape for the AWL, making it more compact). Thus, AWGs take on a "W" shape, and AWL takes on a "U" shape, the opposite of the usual case.

More recently, a highly compact silica waveguide PLC four-channel CWDM multiplexer made using a two-dimensional (2-D) reflective hologram was demonstrated [37].

G. Athermal (Temperature-Insensitive) AWGs

The temperature sensitivity of the passband center wavelength (frequency) in the silica-based AWG is about $d\lambda/dT = 1.2 \times 10^{-2}$ (nm/deg) $(d\nu/dT = -1.5$ (GHz/deg)), which is mainly determined by the temperature dependence of silica glass itself $(dn_c/dT = 1.1 \times 10^{-5}$ (1/deg)). The AWG multiplexer should be temperature controlled with a heater or a Peltier cooler to stabilize the channel wavelengths. This requires a constant power consumption of a few Watts and significant equipment for the temperature control. Various kinds

of AWG configurations to achieve athermal operation have been proposed [38]–[41].

Fig. 25 shows a schematic configuration of an athermal AWG in which the temperature-dependent optical path length change is compensated by the movement of the input fiber position. The input coupling device consists of three parts, namely one part holding the input fiber, an additional post to fix the whole coupling device to the chip, and a metal compensating rod between them. The compensating rod is made of a material with a high thermal expansion coefficient, e.g., aluminum. It changes its length with the ambient temperature T and shifts the input fiber along the endface of the slab waveguide to compensate for the thermal drift of the passband center wavelength in AWG.

Fig. 26 shows the shift of several channels' peak transmissions with temperature for a 200-GHz module. The temperature is varied from $-35\,^\circ$C to $+80\,^\circ$C. The center wavelength of the AWG filter is tuned back to the desired value and becomes nearly independent of the ambient temperature. This method may be applied to spectrographs and phased array filters realized in any material.

Fig. 27 shows a schematic configuration of an athermal AWG without any moving parts. The temperature-dependent optical path difference in silica waveguides is compensated with a trapezoidal groove filled with silicone adhesive that has a negative TO coefficient. Since the passband center wavelength is given by $\lambda_0 = n_c \Delta L/m$, the optical path length difference $n_c \Delta L$ must be made insensitive to temperature. Therefore, the groove is designed to satisfy the conditions

$$n_c \Delta L = n_c \Delta \ell + \hat{n}_c \Delta \hat{\ell} \qquad (21)$$

and

$$\frac{d(n_c \Delta L)}{dT} = \frac{dn_c}{dT}\Delta \ell + \frac{d\hat{n}_c}{dT}\Delta \hat{\ell} = 0 \qquad (22)$$

where $\hat{n}$ is the refractive index of silicone, and $\Delta \ell$ and $\Delta \hat{\ell}$ are the path length differences of silica waveguides and the silicone region. Equation (21) is a condition to satisfy the AWG specifications, and (22) is the athermal condition. The temperature sensitivity of silicone is $d\hat{n}_c/dT = -37 \times 10^{-5}$(1/deg). Therefore, the path length difference of silicone is $\Delta \hat{\ell} \cong \Delta \ell/37$. Fig. 28 shows the temperature dependencies of passband center wavelengths in conventional and athermal AWGs. The temperature-dependent wavelength change has been reduced from 0.95 to 0.05 nm in the $0-85\,^\circ$C range. The excess loss caused by the groove is about 2 dB, which is mainly due to diffraction loss in the groove. The insertion loss caused by diffraction loss can be reduced by segmenting a single trapezoidal silicone region into multiple groove regions [42]. In segmented groove regions, the light beam is periodically refocused. Therefore, the insertion loss is reduced to about 0.4 dB.

H. Tandem AWG Configuration

The maximum available wafer size of a PLC is limited by the fabrication apparatus, such as the deposition machine, electric furnace, mask aligner, etc. Therefore, it is not easy to fabricate AWGs with very large channel counts. One possible way to increase the total number of channels is to use two
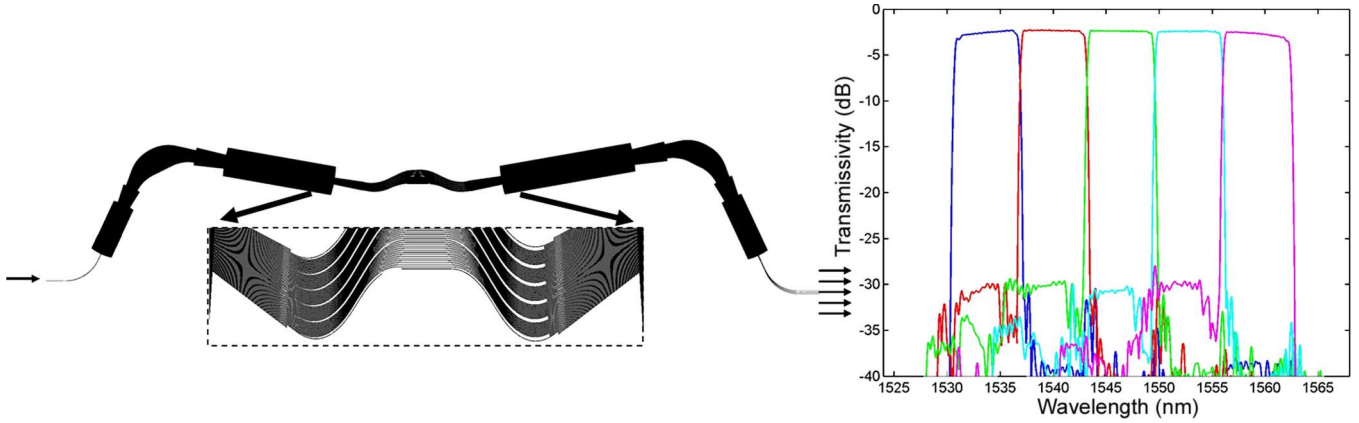
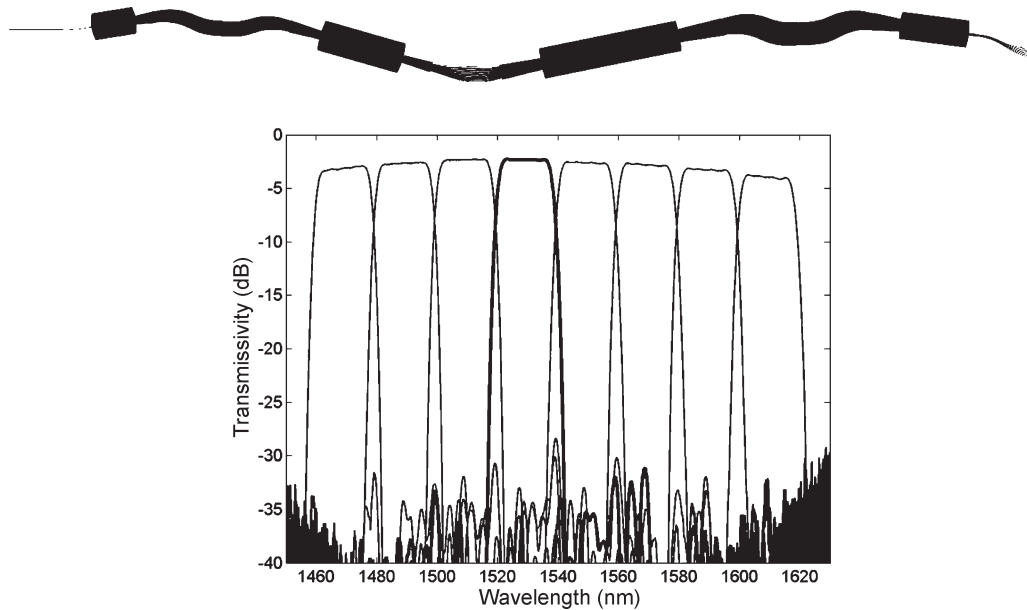Fig. 23. Eight-skip-zero five-band de/multiplexer.
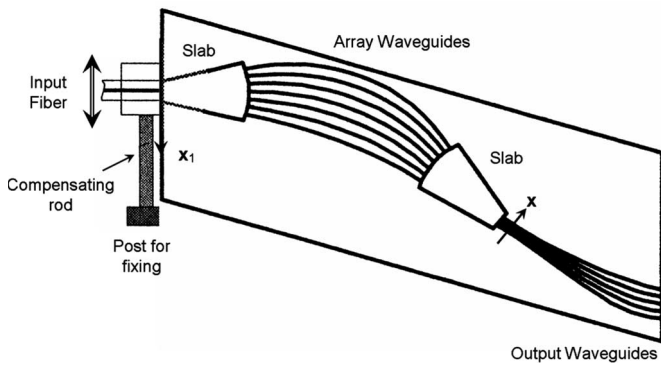

Fig. 24. Eight-channel CWDM de/multiplexer.

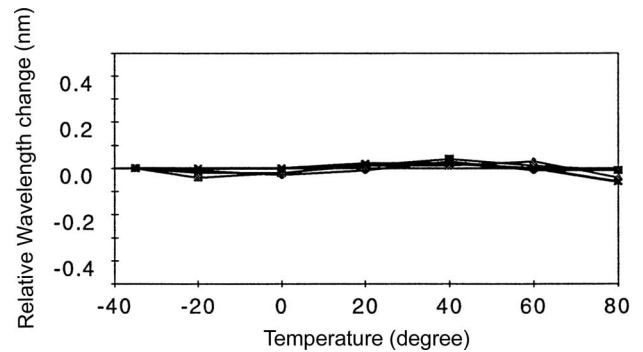Fig. 25. Configuration of athermal AWG with temperature compensating input position.

Fig. 26. Temperature dependences of the passband center wavelengths.

kinds of AWGs, which are cascaded in series. In order to realize much larger channel counts, for example, 1000 channels, a tandem concatenation is important. Fig. 29 shows the configuration of a 10-GHz-spaced 1010-channel WDM filter that covers both C- and L-bands [43]. It consists of a primary 1×10 flat-top AWG (AWG $\#k$ with $k = 1, 2, \ldots, 10$) with a 1-THz channel spacing and ten secondary 1×101 AWGs

with 10-GHz spacing and 200 channels. The crosstalk levels of the secondary AWGs are around -32 dB, and the sidelobe levels in these passbands are less than -35 dB. The tandem configuration enables us to construct flexible WDM systems, that is, secondary AWGs can be added when the bandwidth demand increases. Also, this configuration will be essential for the construction of hierarchical cross-connect (XC) systems such as fiber XC, band XC, and wavelength XC. The output port
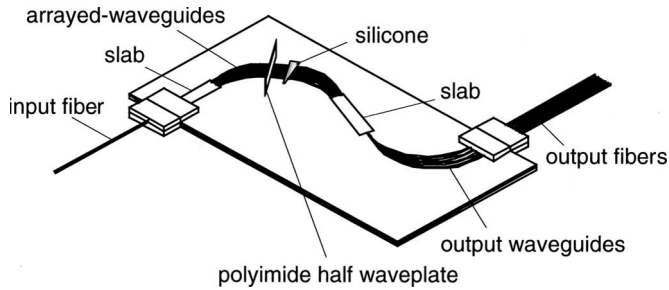
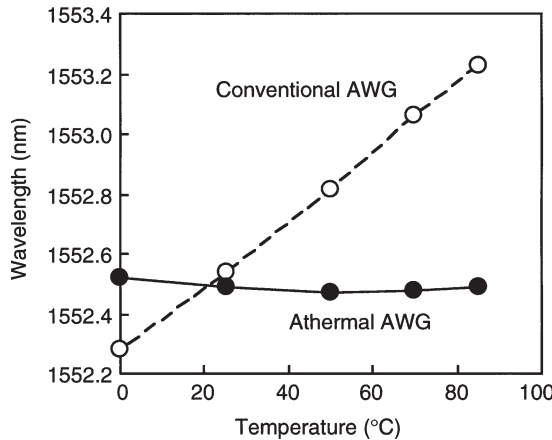Fig. 27. Schematic configuration of silicone-filled athermal AWG.

Fig. 28. Temperature dependences of passband center wavelengths in a conventional AWG and a silicone-filled athermal AWG.

#k ($k = 1, 2, \ldots, 10$) of the primary AWG is connected to the input port of AWG #k through an optical fiber. Two conditions are imposed on these AWGs. First, the center wavelength of 200 channels of AWG #k should be designed to coincide with that of the flat-top passband #k from the primary AWG output #k. Then, passband #k is sliced with the AWG #k without any noticeable loss. Second, the sidelobe components of flat-top passband #k are removed as shown in the inset of Fig. 29. Therefore, one passband within the FSR is obtained from one output port of AWG #k. 101 wavelengths are selected from every AWG #k. Fig. 30 shows the demultiplexing properties of all the channels of the tandem AWG filter. There are a total of 1010 channels, and they are all aligned at 10-GHz intervals with no missing channels in the 1526- to 1608-nm wavelength range. The loss values ranged from 13 to 19 dB. The main origin of the 13-dB loss is the 10-dB intrinsic loss of the primary AWG. This could be reduced by about 9 dB when a 1×10 interference filter is used instead of a flat-top AWG. A 4200-channel AWG with 5-GHz channel spacing has also been fabricated by using the tandem configuration [44]–[46].

I. Chirped AWGs

All of the AWGs discussed so far have had a constant path length difference between adjacent grating waveguides, except for some designs discussed in Section II-D. If we use a variable path length difference, we create a "chirped" AWG. We will discuss two main types of chirped AWGs. The first is where the arm path length versus arm number has a quadratic component. We will call this "quadratic chirping." The second is where

the path-length difference between adjacent arms oscillates between two values. We will call this "interleave chirping."

1) Quadratic Chirping: By adding a significant quadratic component to the arm length distribution and then quantizing it to an integer multiple of a desired wavelength, one can have an imaging focal length in the AWG that changes significantly with wavelength [47], [48]. In other words

$$L(i) = \text{round}(i + \gamma i^2)\Delta L. \tag{23}$$

This can be used to make one grating order have a higher transmissivity than others. This was used to make a tunable laser consisting of silica AWG and a semiconductor optical amplifier oscillate in a desired grating order [49]. If one wishes to have multiple ports in focus simultaneously in a quadratic chirped AWG, one needs to distort the star coupler. One can tilt the focal line of the star coupler at the output ports, vary the grating port pitch linearly, or a combination of both.

2) Interleave Chirping: An interleave-chirped AWG has interleaved sets of grating arm lengths with different properties. Two main types have been demonstrated. One is the different sets of waveguides that have a small difference in their path length difference and have been used to create flat-top passbands in AWGs [50]. This technique necessarily adds insertion loss, however, in accordance with Theorem 1. The other is the different sets of waveguides that have approximately the same path length difference, but there is a phase shift difference between them, and have been used to create a wavelength-selective switch (WSS) [51].

Fig. 31 shows the waveguide layout for the WSS. It consists of two interleave-chirped AWGs connected by an AWL with TO phase shifters in each arm. The odd-numbered grating waveguides in the interleaver-chirped AWGs have a $\lambda/4$ extra path length as compared to the even-numbered grating waveguides. This causes two images to be generated by the AWG at each wavelength. The AWL is connected to pick up these two images plus one extra image from outside the central Brillouin zone. Thus, there are three images per wavelength channel. There are two input waveguides and two output waveguides for the WSS. By controlling the relative phases between the three images for each channel, each channel can be routed independently from either input waveguide to either output waveguide. The three phases help provide an improved extinction ratio. Fig. 31 shows the measured transmissivity for one switching state. Although this WSS has a low insertion loss and is compact, the thermal crosstalk between phase shifters in the WSS makes it difficult to control.

III. INTERSIGNAL CONTROL DEVICES

Intersignal control devices can power regulate and route wavelength channels in WDM networks.

A. ROADMs

A ROADM is a device that gives simultaneous access to all wavelength channels in WDM communication systems. The first PLC integrated-optic ROADM was fabricated, and basic functions of individually routing 16 different wavelength
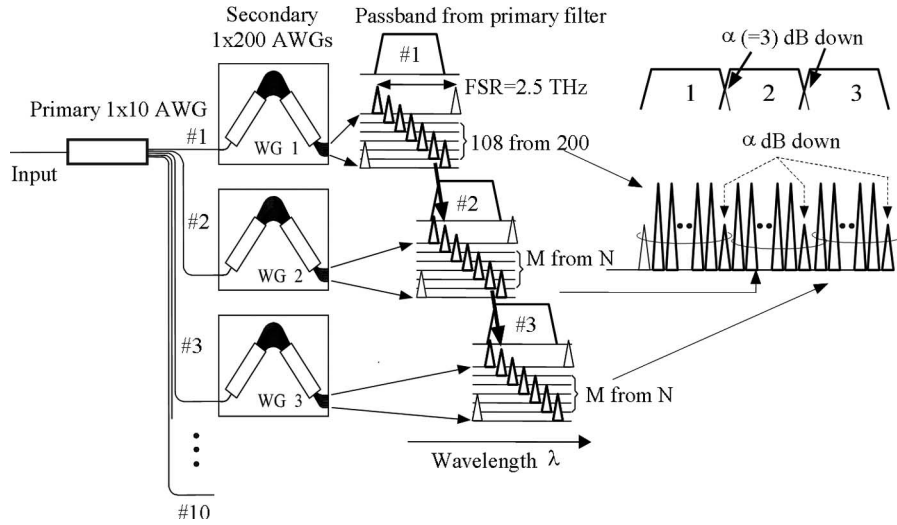
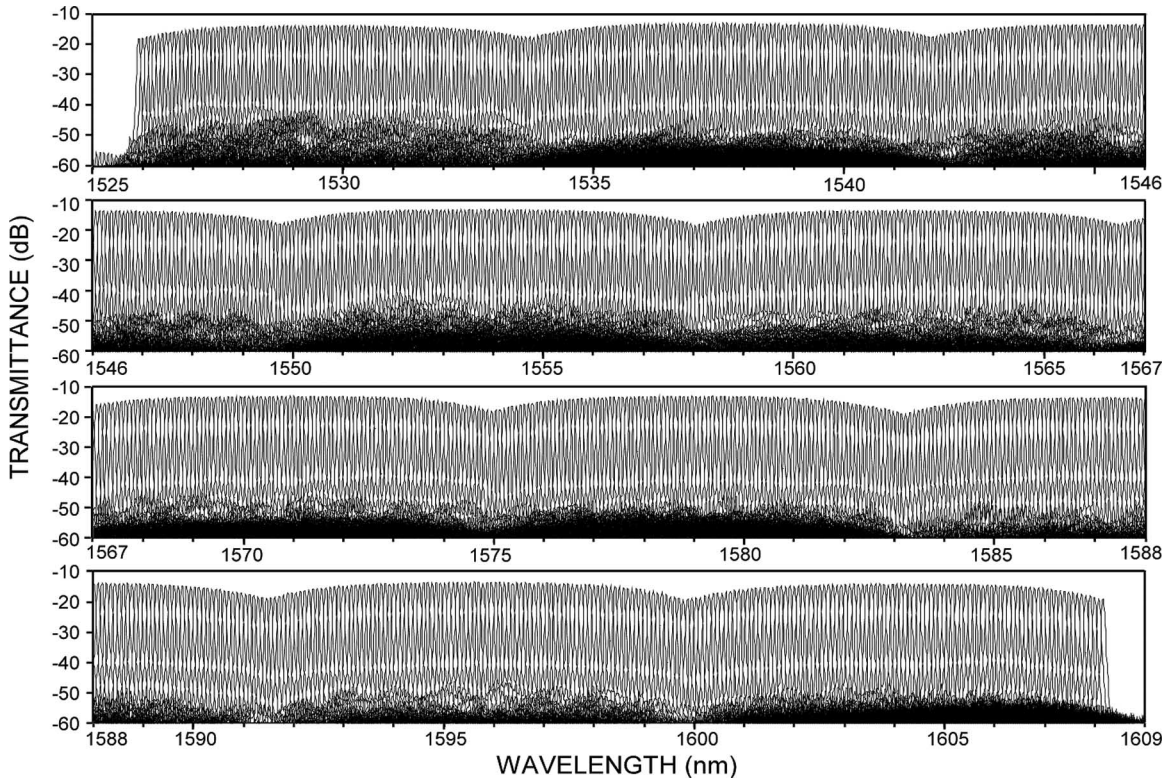Fig. 29.   Configuration of 10-GHz-spaced 1010-channel tandem AWG.

Fig. 30.   Demultiplexing properties of all the channels of the tandem AWG filter.

channels with 100-GHz channel spacing were demonstrated in [52]. The waveguide configuration of the 16-channel optical ROADM is shown in Fig. 32. It consists of four AWGs and 16 double-gate TO switches (TOSWs). Four AWGs are allocated with crossing their slab regions with each other. These AWGs have the same grating parameters; they are the channel spacing of 100 GHz and the FSR of 3300 GHz (26.4 nm) in the 1.5-μm region. Equally spaced WDM signals, $\lambda_1, \lambda_1, \ldots, \lambda_{16}$, which are coupled to the main input port (add port) in Fig. 32, are first demultiplexed by the $AWG_1(AWG_2)$, and then 16 signals are introduced into the left-hand-side arms (right-hand-side arms) of double-gate TOSWs. The crossing

angle of the intersecting waveguides are designed to be larger than $30°$ to make the crosstalk and insertion loss negligible.

Here, the "OFF" state of a double-gate switch is defined as the switching condition where a signal from a lower left input port (right input port) goes to an upper right output port (left output port) in Fig. 32. The "ON" state is then defined as the condition where a signal from a lower left input port (right input port) goes to a lower left output port (right output port). When a double-gate switch is "OFF," the demultiplexed light by $AWG_1(AWG_2)$ goes to the cross arm and is multiplexed again by $AWG_3(AWG_4)$. On the other hand, if a double-gate switch is "ON" state, the demultiplexed light by $AWG_1(AWG_2)$
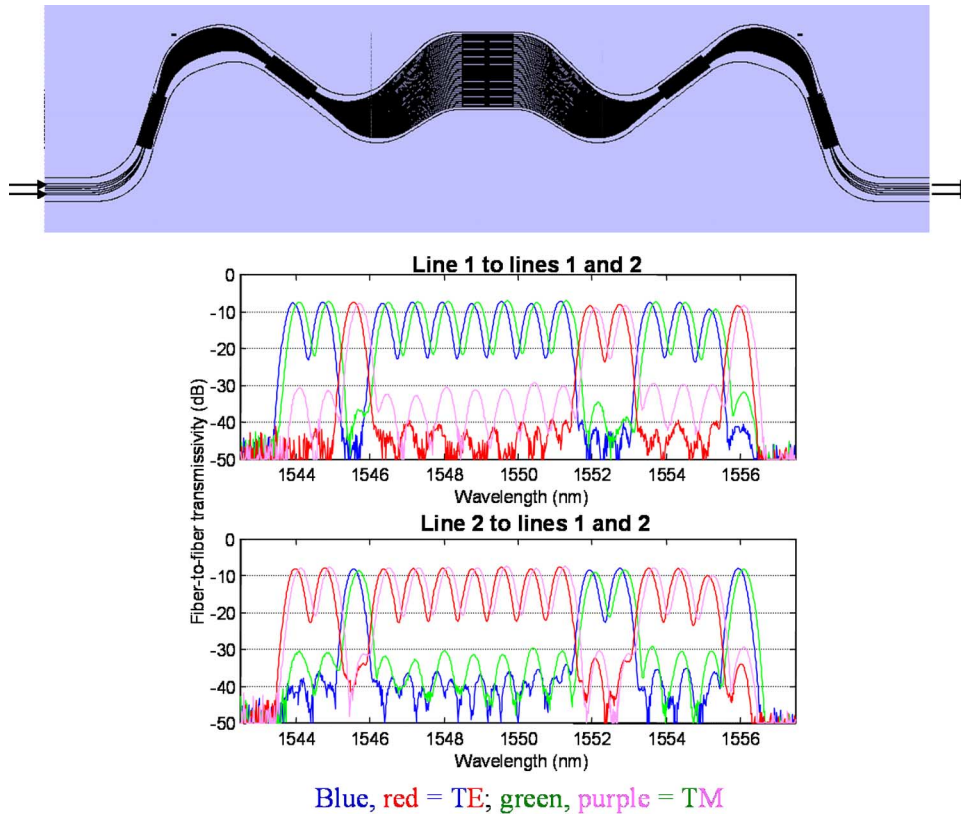
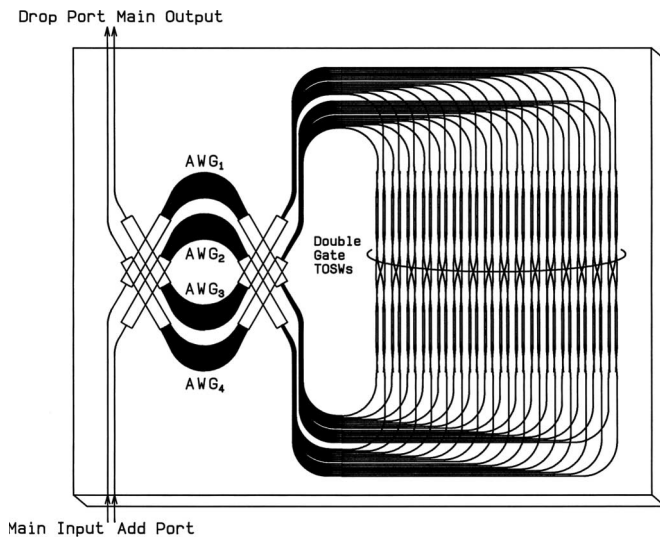Fig. 31. WSS made using two interleave-chirped AWGs and an AWL.

Fig. 32. Waveguide configuration of 16-channel ROADM with double-gate TOSWs.

Fig. 33. Transmission spectra from main input port to main output port (solid line) and drop port (dotted line) when all TOSWs are "OFF."

goes to the through arm and is multiplexed by $AWG_4(AWG_3)$. Therefore, any specific wavelength signal can be extracted from the main output port and led to the drop port by changing the corresponding switch condition. Signals at the same wavelength as that of the dropped component can be added to the main output port when it is coupled into the add port in Fig. 32.

Fig. 33 shows the light transmission characteristics from the main input port to the main output port (solid line) and drop port (dotted line) when all TOSWs are "OFF." The ON–OFF crosstalk is smaller than -33 dB with on-chip losses of 7.8–10.3 dB.
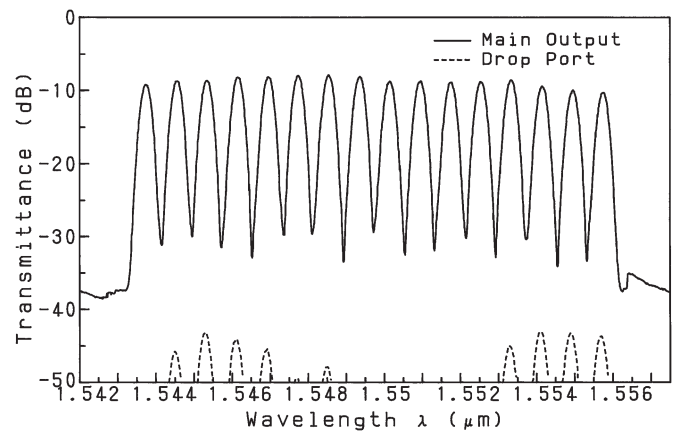
When TOSWs SW_2, SW_4, SW_6, SW_7, SW_9, SW_{12}, SW_{13}, and SW_{15}, for example, are turned "ON," the selected signals λ_2, λ_4, λ_6, λ_7, λ_9, λ_{12}, λ_{13}, and λ_{15} are extracted from main output port (solid line) and led to the drop port (dotted line), as shown in Fig. 34. The ON–OFF crosstalk is smaller than -30 dB with on-chip losses of 8–10 dB. Since optical signals pass through both AWG_3 and AWG_4, the crosstalk level here is determined by the crosstalk in the arrayed waveguides.

Fig. 35 shows the waveguide configuration of an athermal 16-channel ROADM [53]. The silicone-type athermal technique is incorporated in this ROADM. Transmission spectra become essentially insensitive to temperature change, as shown in Fig. 36.
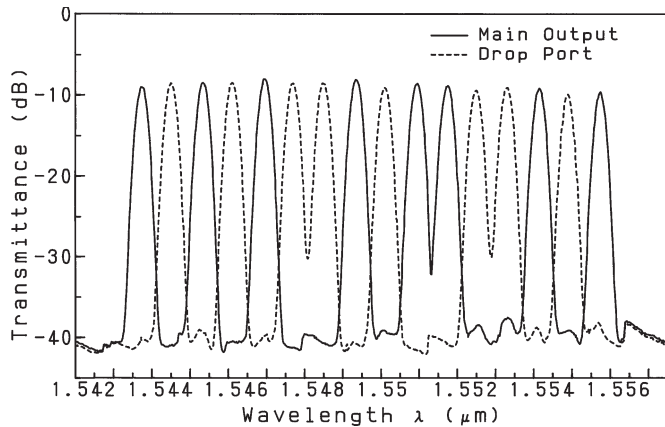
Fig. 34. Transmission spectra from main input port to main output port and drop port when TOSWs SW_2, SW_4, SW_6, SW_7, SW_9, SW_{12}, SW_{13}, and SW_{15} are "ON."
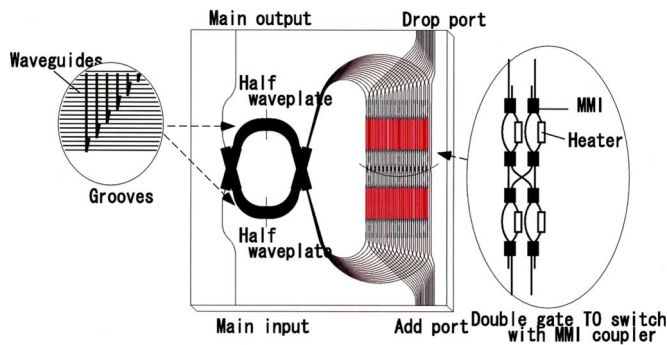

Fig. 35. Configuration of athermal 16-channel ROADM.

Although the electric power necessary to drive a double-gate switch is two times larger than the conventional TOSW, the power consumption itself can be reduced to almost 1/5 to 1/2 when bridge-suspended phase shifters [54] or a trench/groove structure [55] is utilized. The present ROADM can transport all input signals to the succeeding stages without inherent power losses. Therefore, these ROADMs are very attractive for all optical WDM routing systems and allow the network to be transparent to signal formats and bit rates.

B. Large-Channel Count ROADMs

The first demonstrated PLC ROADM was discussed above in Section III-A. This 16-channel demonstration has numerous waveguide crossings, which can require significant wafer real estate. To scale to a very large channel count, a reflective design using a striped mirror facet was demonstrated [56]. This design had through passbands with two zero-loss maxima by employing two waveguides per channel. One design used perfect spectral sampling across the entire spectrum to achieve no gaps between through channels, as shown in Fig. 37. A difficulty with this design is that after fabrication, one had to manually trim the phases in all the waveguides using electrical hyperheating to phase align all the spectral components. Another design that is easier to manufacture used perfect spectral sampling only in pairs [57]. In this case, only the phase alignment within each pair needed to be trimmed. However, the full flat passband between adjacent through channels was lost. Yet another design
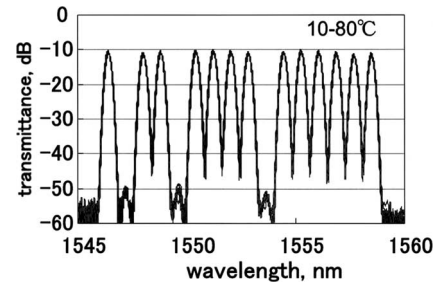

Fig. 36. Transmission spectra of athermal 16-channel ROADM.

used an MZI input to create a 64-channel colored ROADM with flat-top passbands (as described in Section II-E2), as shown in Fig. 38 [58]. In this case, only one phase alignment in the entire device (the MZI to the AWG) needed to be performed.

C. WSSs

A $J \times K$ WSS is a device that routes WDM signals from J inputs to K outputs and can be used to make a ROADM. There are many different types. We showed a 2×2 WSS in Section II-I2. The most common type is a $1 \times K$ WSS. A 1×1 WSS is called a blocker. It can either block or pass each WDM channel that passes through it. Several PLC blocker demonstrations have been reported [59]. A $1 \times K$ WSS can be used to create a colorless ROADM or an optical mesh node.

Fig. 39 shows a waveguide layout of a 1×9 WSS [60]. It uses a tree arrangement of 1×2 TOSWs and a final stage of shutters for improved switching extinction ratio and also to provide a variable optical attenuation (VOA) function. It also includes a star coupler with eight VOAs to act as an add channel combiner. Furthermore, it includes an interleaver and a de-interleaver.

This 1×9 WSS PLC, along with a band de/multiplexer PLC, was developed to create a modular 80-channel ROADM, as shown in Fig. 40 [61].

IV. INTRASIGNAL CONTROL DEVICES

Intrasignal control devices can modify the waveforms of optical signals in order to create desired pulse shapes, overcome transmission impairments, etc.

A. Temporal Pulse Waveform Shapers

The shaping and encoding of optical pulse waveforms are important for a variety of applications in optical communications, optical radar, and picosecond and femtosecond spectroscopy. Control of the pulse temporal profile is achieved by spatially dispersing the optical frequency components, whose amplitude and phase are arbitrarily weighted, and multiplexing them again into a single optical beam. Weiner *et al.* [62] first demonstrated a technique for optical pulse shaping using a grating pair as a dispersive element and masks for amplitude and phase filtering. Since they used a grating pair, the size of the experimental apparatus was of the order of 1 m^2. Also, the weighting functions for the amplitude and phase masks were fixed because they fabricated them by metal deposition and reactive-ion etching of the silica glass.
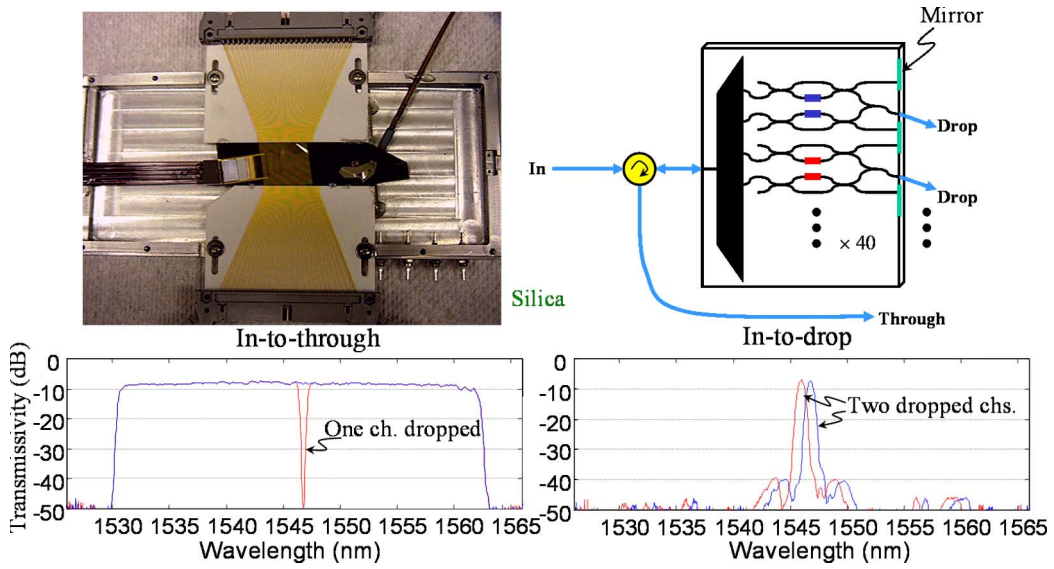
Fig. 37. Forty-channel reflective ROADM using an AWG with perfect spectral sampling.
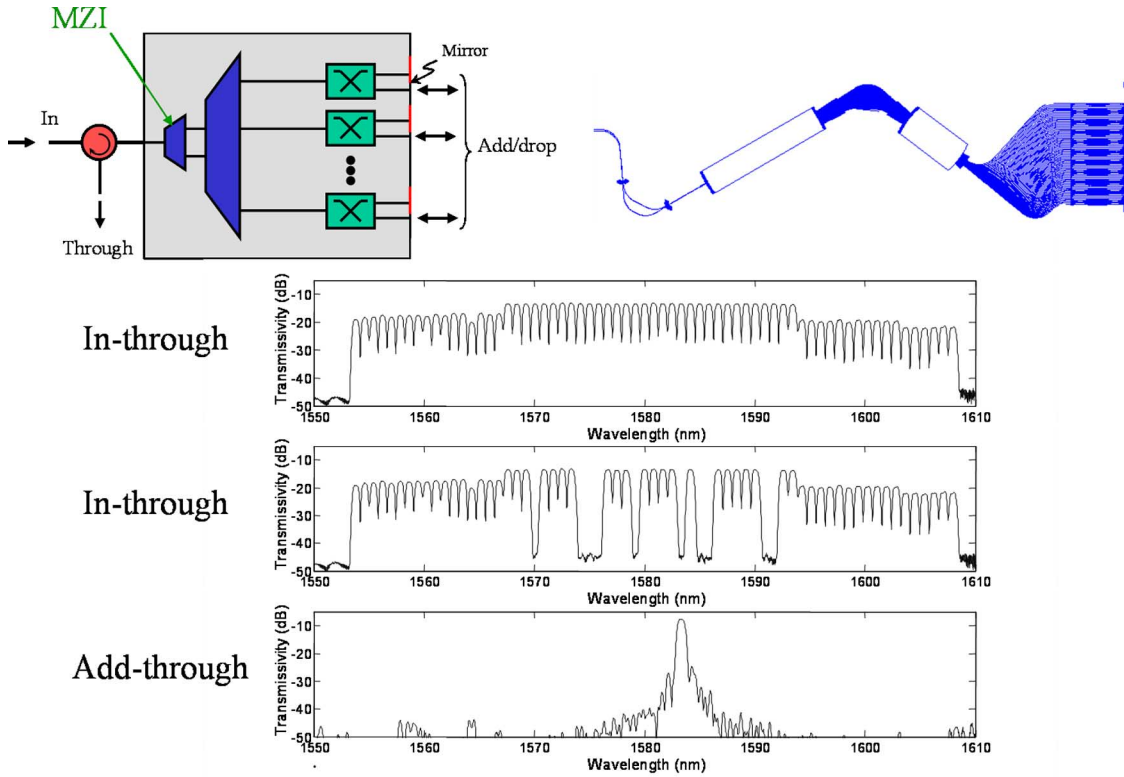

Fig. 38. Sixty four-channel reflective ROADM using an MZI input to the AWG.
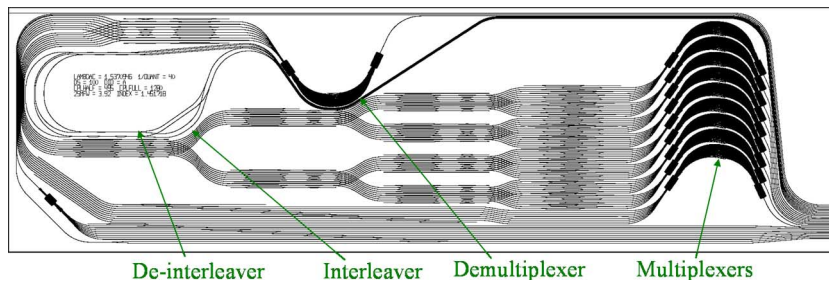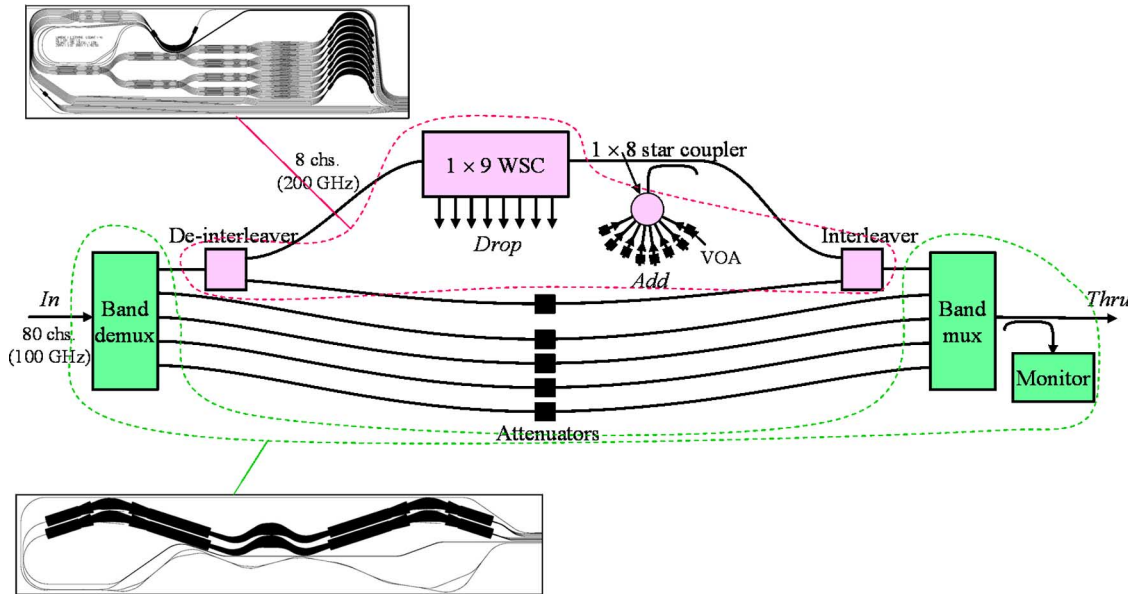

Fig. 39. Eight-channel 1 × 9 WSS.

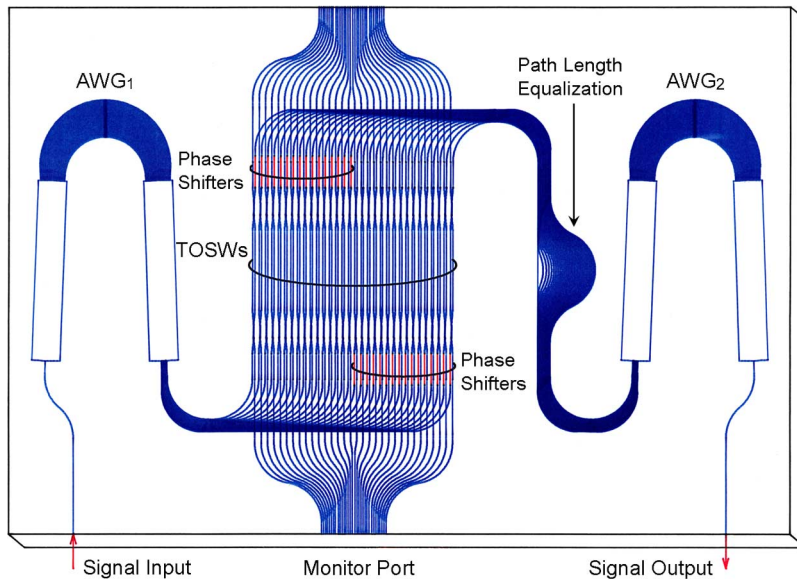Fig. 40.   Modular 80-channel partially colorless ROADM.

Fig. 41.   Schematic configuration of temporal pulse waveform shaper.

A schematic configuration of a fully integrated optic dynamic temporal pulse waveform shaper is shown in Fig. 41 [63]. It consists of an AWG pair for demultiplexing (AWG_1) and multiplexing (AWG_2) the spectral components of mode-locked optical pulses and TOSWs and phase shifters for arbitrarily patterning the spectral components. The channel spacing and total number of channels of the AWG are 40 and 80 GHz, respectively, which are centered at $\lambda_0 = 1.55$ μm. Thirty two channels among 80 channels of the AWG are used for spectral filtering. An array of 32 TOSWs and phase shifters is allocated between the AWG pair. All of the optical path lengths from AWG_1 to AWG_2 are made equal by employing path adjustment waveguides. The switching ratio of each TOSW, which can be controlled essentially from 0 to 1, is measured by using the monitor port. Also, the amount of phase shift in each path is determined by comparing the relative phase difference with a reference arm, which is not shown in Fig. 41. The fiber-to-

fiber insertion loss is 12 dB, and the extinction ratio is about 30 dB. The average electric power for each TOSW is about 300 mW. The minimum controllability of the electric power is 1–2 mW. This enables us to obtain 0.1- to 0.2-dB amplitude controllability. The average electric power necessary to obtain π phase shift is also about 300 mW. According to this minimum controllability of electric power, the phase shifter resolution is about $\pi/100$.

The temporal pulse waveform shaper can be utilized in a variety of applications for optical pulse multiplexing, pulse waveform shaping, frequency chirping compensation, and frequency-encoding code division multiplexing. N times optical pulse multiplication can easily be accomplished by filtering the line spectral components of the mode-locked pulse in every Nth interval.

A square-shaped optical pulse is a particularly useful pulse shape with potential application to nonlinear optical metrology,
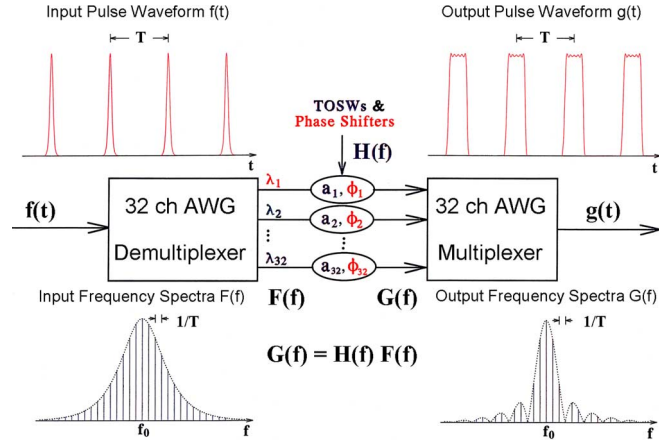
Fig. 42. Schematic pulse waveforms and frequency spectra in square pulse generation scheme.

coherent transient spectroscopy, and future all-optical switching and optical demultiplexing [64], [65]. Fig. 42 shows the schematic temporal pulse waveforms and frequency spectra in the square pulse generation scheme. The frequency spectrum of a mode-locked pulse train with the waveform $f(t) = A \cdot \text{sech}(t/t_0)$ is given by

$$F(f) = \sum_{m=-\infty}^{\infty} A \cdot \text{sech}\left[\pi^2 t_0 (f - f_0)\right] \delta\left(f - f_0 - \frac{m}{T}\right) \quad (24)$$

where f_0, T, and t_0 denote center frequency, pulse interval, and pulse width (full-width at half-maximum (FWHM) width $\tau = 2\cosh^{-1}\sqrt{2} \cdot t_0 \cong 1.763 t_0$), respectively. In order to generate square pulses with rise and fall times of $(t_2 - t_1)$, the corresponding sinc-like frequency spectra with the form

$$G(f) = \sum_{m=-\infty}^{\infty} \frac{\sin\left[\pi(t_2 + t_1)(f - f_0)\right]}{\pi(t_2 + t_1)(f - f_0)}$$
$$\cdot \frac{\cos\left[\pi(t_2 - t_1)(f - f_0)\right]}{1 - \left[2(t_2 - t_1)(f - f_0)\right]^2} \cdot \delta\left(f - f_0 - \frac{m}{T}\right) \quad (25)$$

should be synthesized. Then, the amplitude and phase weighting function of the $H(f)$ pulse shaper for each spectral component are determined by $H(f) = G(f)/F(f)$. Here, we assume $T = 25$ ps, $\tau = 8$ ps, $t_1 = 3.3$ ps, $t_2 = 5.3$ ps, and $f_0 = 1.931$ THz ($\lambda_0 = 1.552524$ μm).

Fig. 43(a) and (b) shows the experimental original spectra and autocorrelated pulse waveforms [66]. The original pulse had an FWHM of $\tau = 0.9$ ps whose autocorrelation is shown in Fig. 43(b). Fig. 44(a) and (b) shows the synthesized spectra and corresponding cross-correlated pulse waveforms for the designed pulse widths of $\tau = 11.9$ ps. Dotted and solid lines show designed and experimental values, respectively. The ripples in the flat-top pulse region are caused by the finite available bandwidth and are estimated to be 0.1 dB compared with the calculated values of 0.2 dB. The rise and fall times (10%–90%) are 2.9–5.4 ps, while the designed values are both 1.5 ps. The deterioration in the rise and fall times is mainly brought about by phase setting errors that originated in the thermal crosstalk among the phase shifters used for TO phase adjustment. Phase setting errors could be reduced by using heat-insulating grooves.

B. General Optical Equalizers

An equalizer is a device that at least partially restores a signal corrupted by deterministic intersymbol interference (ISI). ISI is the mixing together of portions of the signal from different keying intervals. An example source of ISI is chromatic dispersion in optical fiber. Equalizers successfully undo only deterministic ISI and not random processes, such as spontaneous emission from amplifiers. Equalizers in the electrical domain are a well-known and widely used technology. The electrical technology is called electrical equalization. Here, we will focus on optical equalization (OEQ).

The simplest type of equalizer is a tapped delay line. A tapped delay line consists of a series of weighted taps and delays that are readded to the signal. Adjusting the weights' amplitudes and phases allows one to create a desired impulse response. Ideally, this impulse response is the inverse of the impulse response that created the ISI, i.e., $h_{\text{EQ}}(t) = F^{-1}\{1/F\{h_{\text{ISI}}(t)\}\}$. To create a tapped delay line in optics, one can use MZIs, as demonstrated in [67].

Fig. 45 shows an extremely simple OEQ, i.e., a two-tap OEQ, with one precursor tap and one postcursor tap. For many ISI impairments, it is found that the best time tap spacing is ~0.7 times the bit period of the digital data signal. Fig. 45 shows the waveguide layout using TO adjustable couplers and phase shifters. Two-tap OEQs have been demonstrated for both 40- and 100-Gb/s signals, correcting modulation bandwidth limitations, extinction ratio limitations, chromatic dispersion, and signal distortion due to narrow optical filtering. They have also been shown to mitigate PMD impairments by signal shaping. By making the OEQ have an FSR that aligns with the WDM channel spacing, a plurality of WDM channels can be equalized simultaneously, provided the ISI on the channels is equal. It is important to realize that equalization reshapes not only the signal but also the noise. In general, it is better to equalize the signal when the optical-signal-to-noise ratio is high.

Such a two-tap OEQ, with a time tap spacing of 7 ps, was used to compensate ISI due to modulator bandwidth limitation and achieve a high-quality 107-Gb/s nonreturn-to-zero signal [68], as shown in Fig. 46.

C. Optical Chromatic Dispersion Compensators

An optical dispersion compensator (ODC) is an optical equalizer optimized to compensate chromatic dispersion. It is often used to compensate the chromatic dispersion encountered in optical fibers. Standard single-mode fiber has a dispersion of ~ +17 ps/nm/km in the C-band. If the amount of dispersion is adjustable, we will call the device a tunable ODC (TODC).

Let us define a figure of merit for a TODC, which is the usable bandwidth squared multiplied by the dispersion adjustment range. This can be made nondimensional, and the signal bandwidth squared multiplied by dispersion is an approximate number of bit slots that each bit is spread across by the dispersion.

D. IIR

An IIR filter is a filter with an infinite number of impulses and is optically created using one or more resonators. Chromatic dispersion in optical fiber comes from both material
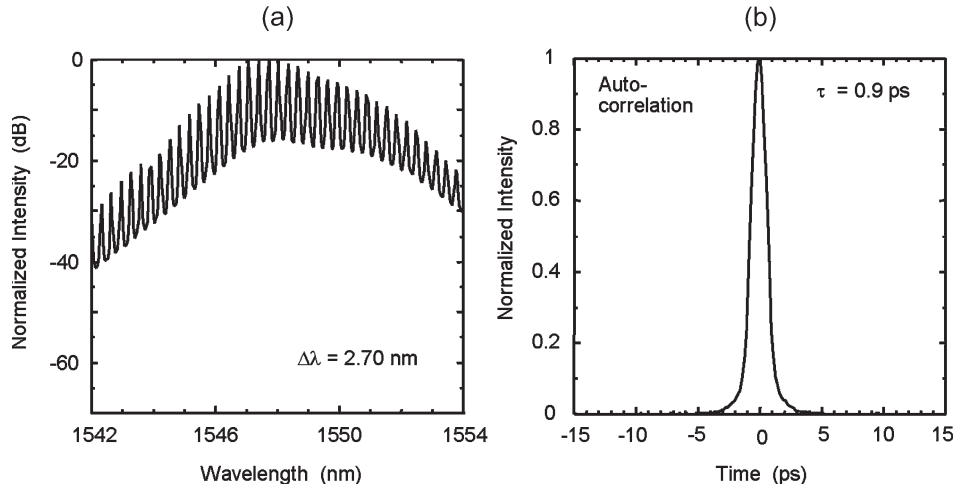
Fig. 43.   (a) Experimental original spectra and (b) autocorrelated pulse waveforms.
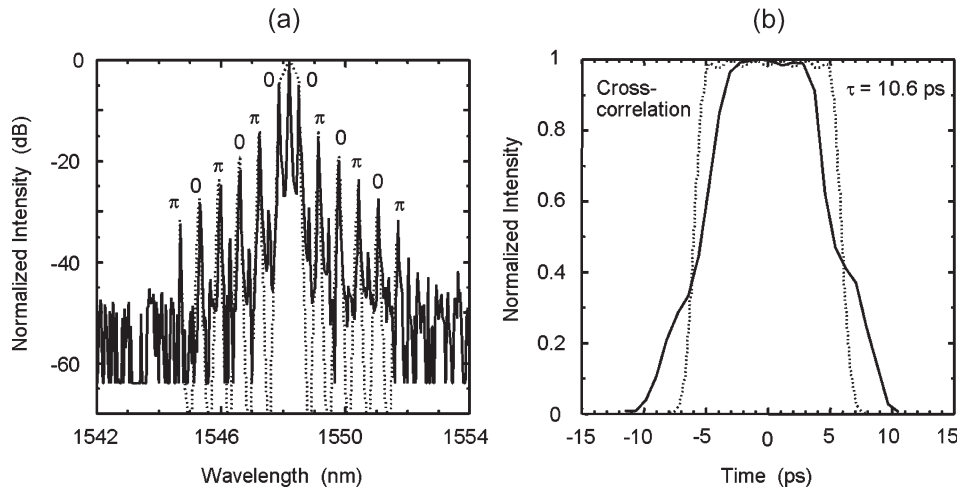
Fig. 44.   (a) Synthesized spectra and (b) corresponding cross-correlated pulse waveforms for designed pulse widths of $\tau = 11.9$ ps.
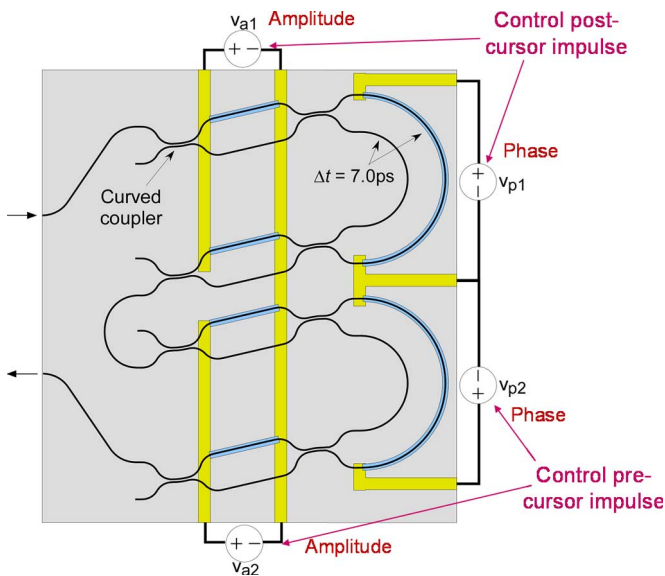
Fig. 45.   Two-tap general OEQ.

effects and waveguiding effects. Both are resonant in nature and thus have an IIR. It is natural to try to equalize them with another IIR filter.
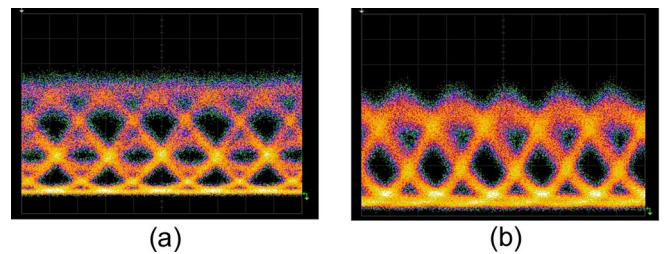
Fig. 46.   One hundred seven-Gb/s eye diagram (a) before and (b) after OEQ.

A convenient way to make an IIR dispersion compensator is to use an all-pass filter [69]. An all-pass filter is an IIR filter with constant unity transmissivity but a nonlinear phase response as a function of optical frequency. A good example is a waveguide coupled to a ring resonator. If the waveguide, coupler, and ring resonator are lossless, then there is no loss going through the waveguide. However, light that has an optical frequency that is resonant in the ring will take a longer time to pass through the waveguide. Thus, the group delay will exhibit one peak each ring FSR. By placing several rings in series, all coupled to the same waveguide, and controlling the ring coupling and length, one can create an approximately linear region of group
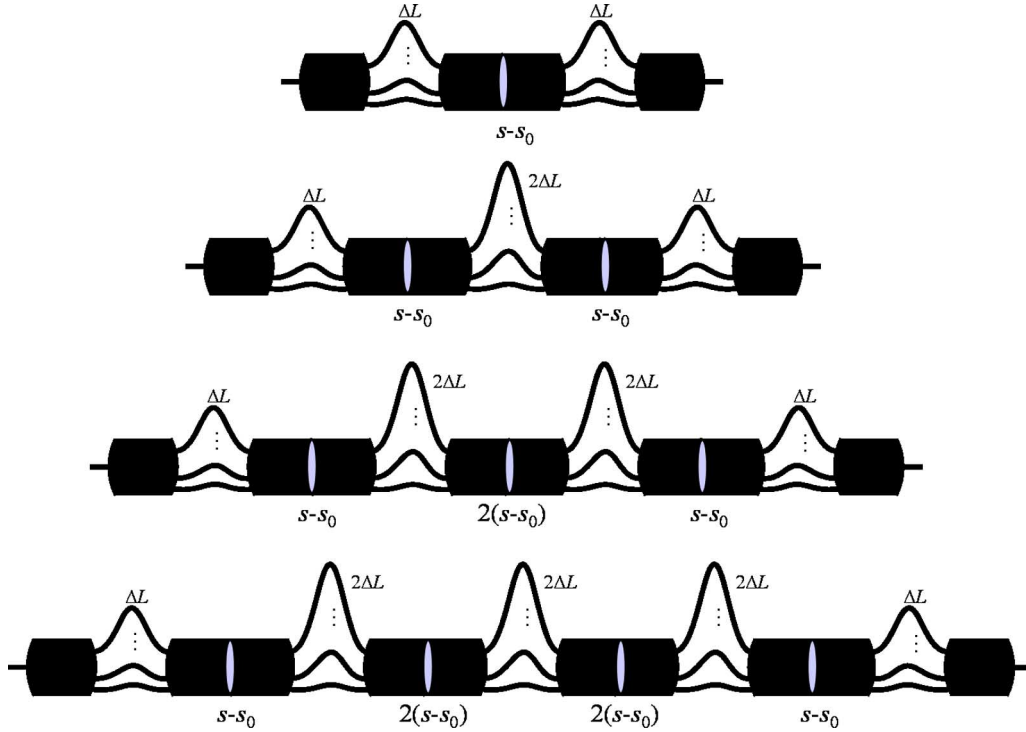
Fig. 47. FIR TODC designs that do not require interferometer phase shifting and the dispersion can be adjusted by a single control knob.

delay, thus generating chromatic dispersion, which can be used to equalize the dispersion encountered in the optical fiber.

E. Finite Impulse Response (FIR)

One can also do a significant amount of dispersion compensation using an FIR filter [70]. There is no all-pass FIR filter, so the filter must be designed to have both a linear group delay and a constant transmissivity over the bandwidth of interest. Optically, we can construct them out of interferometers, e.g., MZIs, AWGs, etc.

1) Two-Stage-Type TODC: In the general OEQ section, we presented a device that could be used as a dispersion compensator, consisting of two single-stage MZIs. To create an improved compensator, we will need to create multiple low-loss maxima. Thus, according to Theorem 1, we will need to use multiple inputs and outputs of couplers. Although there are many possible designs, we will focus on the designs shown in Fig. 47. The advantages of these designs are that they do not require any phase shifting in the arms of the length-imbalanced interferometers, and they can be driven by a single control knob. The simplest is the topmost design in Fig. 47.

This TODC design consists of two AWGs connected at their second star coupler outer boundaries (where output waveguides would normally be connected). The frequency response measured from input to output has a Gaussian-shaped passband with a constant negative chromatic dispersion, where dispersion given by

$$D_0 = \frac{-2Rf}{n(a\Delta f)^2} \quad (26)$$

where R is the star coupler radius, n is the refractive index in the slab, a is the grating waveguide pitch at the star coupler,

f is the optical frequency, and Δf is the AWG FSR. It is usually best to make Δf equal to the WDM channel spacing.

To understand why the device has a negative dispersion, consider the lower part of Fig. 48. The center lines of the Gaussian beams for three different wavelengths within an FSR are shown. From the left-hand AWG, the wavelengths are focused onto the middle of the double star coupler. Wavelengths longer than the channel center wavelength are imaged below, while the shorter wavelengths are imaged above. After passing the focal line, these beams continue in a straight line, and when they reach the grating arms of the second AWG, they are no longer centered. Because the effective path length through an AWG is equal to the average of the path lengths weighted by the power in each path, longer wavelengths end up traveling a shorter path than shorter wavelengths. This is negative dispersion. Note that the off-center beams end up coupling to the output waveguide with a reduced efficiency, and thus, the net passband has a rounded single-maxima shape.

To tune the dispersion amount, one needs a lensing action as shown at the lower right in Fig. 48. For example, if a lens with a focal length equal to $R/2$ is placed in the double star center, all the beams are recentered on the grating arms of the second AWG, and the device exhibits zero dispersion. In such a case, the passband is ideally perfect flat, having numerous zero-loss maxima.

One way to create the adjustable lens is to use TOs. Since all angles are much less than 1 rad, a lens is just a quadratic index distribution. One way to create a quadratic index distribution is to drive an array of closely spaced heaters in parallel with a quadratic variation in width. Fig. 48 shows such a device [71].

However, the electrical power consumption of such a lens when using a silica on a silicon substrate can be quite high. In
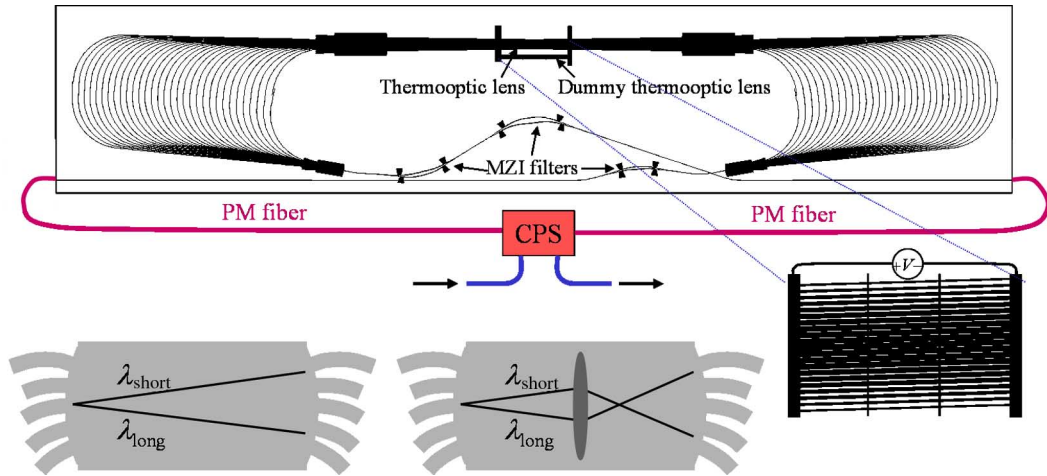
Fig. 48. Two-stage M-arm TODC using a silica TO lens.

the case above, the power consumption was ~ 7 W to tune the entire range.

One way to reduce the power consumption is to cut the design in half and make it reflective. This cuts the power consumption in half. To further reduce it, one can use either a deformable mirror [72] or a polymer TO lens, as shown in Fig. 49 [73]. Polymer gives a large power reduction because the magnitude of its index change with temperature is ~ 30 times that of silica, and the thermal conductivity of polymer is ~ 8 times less than that of silica.

2) Three-Stage-Type TODC: To increase the TODC figure of merit, one can either add grating arms to the AWGs or use more interferometer stages, as shown in Fig. 47. A useful case is reducing the AWG grating arm number to two. In such a case, the AWGs reduce to MZIs, and one can use directional couplers instead of star couplers. Then, the TO lens becomes a simple adjustable coupler.

Fig. 50 shows such a two-arm three-stage TODC. In this example, the bandwidth was chosen very narrow to achieve a large dispersion range. Because of the narrow bandwidth, a filter was integrated with the TODC to use for having the TODC track the signal wavelength. A feedback loop adjusts the TODC temperature to keep it centered on the signal wavelength. The TODC FSR is chosen quite small so that the temperature change required to lock onto any wavelength is at most $\pm 8\,^\circ$C [74].

3) Four-Stage-Type TODC: So far, we have discussed a two-stage M-arm TODC and a three-stage two-arm TODC. We can continue the trend of adding more stages. Here, we discuss a four-stage two-arm TODC. Fig. 51 shows the waveguide layout and measured results from a 100-GHz FSR version [75]. It can compensate $\sim \pm 200$ ps/nm for 40-Gb/s signals. A 33.3-GHz FSR version has also been demonstrated. It can compensate $\sim \pm 2000$ ps/nm for 10-Gb/s signals.

V. Conclusion

In summary, we gave an overview of progress in silica waveguide PLCs to date. We discussed AWGs and their many variations and uses. We discussed intersignal control devices,
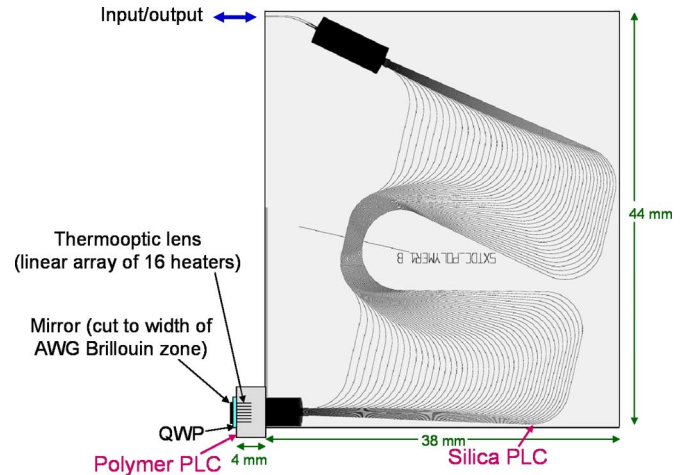
Fig. 49. Two-stage M-arm TODC using a polymer TO lens in a reflective configuration.

such as ROADMs and WSSs, and intrasignal control devices, such as optical equalizers. We apologize that we could present only a small sample of the published PLC devices.

For the future, we expect silica waveguide PLCs to thrive in several areas in the marketplace. For wavelength de/multiplexers, we expect to see more complex AWG structures with lower insertion loss and more rectangular-shaped passbands. For intersignal control devices, we expect to see PLC ROADMs with reduced insertion loss, form factor, and price. Later, we expect to see PLC WSSs with larger channel and/or port counts as networks become more mesh like. For intrasignal control devices, we expect to see PLC dispersion compensators and optical demodulators. Later, we expect to see PLC optical equalizers and pulse shapers.

To enable these advances of actually deployed devices, one of the most important issues is the reduction of power consumption. Silica waveguide TOs, in general, consume significant electrical power and limit the integration density due to thermal management issues. More breakthroughs are needed here. Recent demonstrations of thermal isolation grooves or of hybrid integration with microelectromechanical systems or polymers show possible directions.

Fig. 50.   Three-stage two-arm TODC with integrated wavelength-locking monitor.

Fig. 51.   Four-stage two-arm TODC.

There are, of course, other PLC technologies to consider besides silica waveguides, such as semiconductors (GaAs, InP) [76], 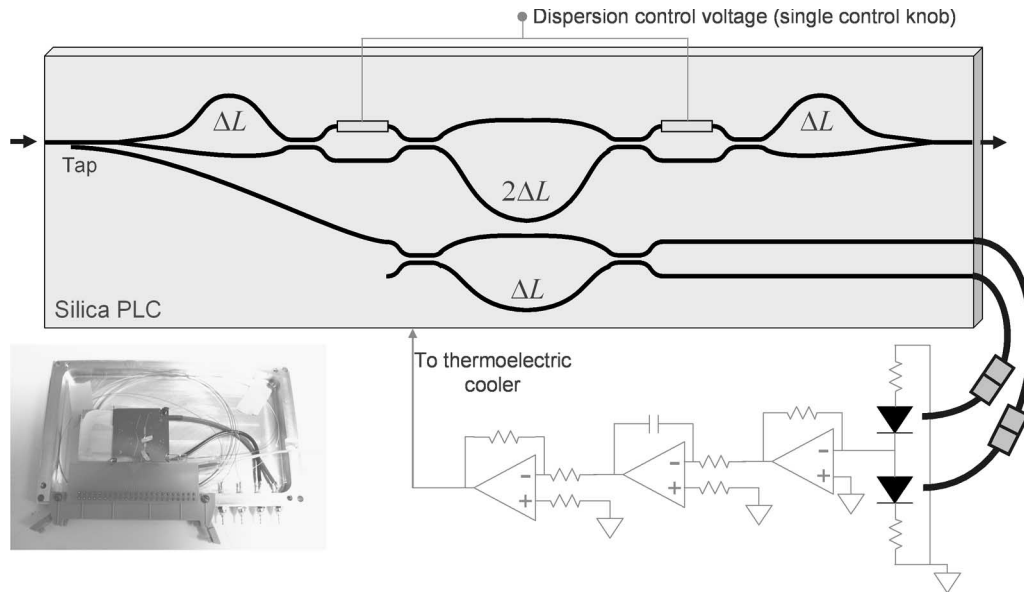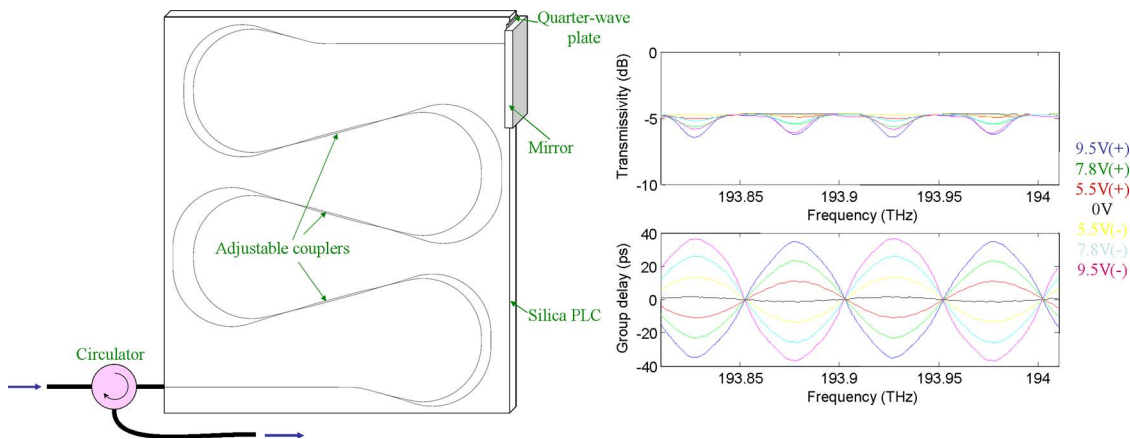polymers [77], silicon oxy-nitride (SiON) [78], lithium niobate $(LiNbO_3)$ [79], and silicon-on-insulator [80], and each will undoubtedly find its own niche, but it is difficult to believe that silica waveguide PLCs will be completely replaced by another technology any time soon because of silica's extreme robustness, very low loss, and near perfect match to optical fiber, which is also made of silica.

REFERENCES

[1] M. K. Smit, "New focusing and dispersive planar component based on an optical phased array," *Electron. Lett.*, vol. 24, no. 7, pp. 385–386, Mar. 1988.

[2] H. Takahashi, S. Suzuki, K. Kato, and I. Nishi, "Arrayed-waveguide grating for wavelength division multi/demultiplexer with nanometer resolution," *Electron. Lett.*, vol. 26, no. 2, pp. 87–88, Jan. 1990.

[3] C. Dragone, C. A. Edwards, and R. C. Kistler, "Integrated optics $N \times N$ multiplexer on silicon," *IEEE Photon. Technol. Lett.*, vol. 3, no. 10, pp. 896–899, Oct. 1991.

[4] M. K. Smit and C. Van Dam, "PHASAR-based WDM-devices: Principles, design, and applications," *IEEE J. Sel. Topics Quantum Electron.*, vol. 2, no. 2, pp. 236–250, Jun. 1996.

[5] Y. P. Li and C. H. Henry, "Silicon optical bench waveguide technology," in *Optical Fiber Telecommunications IIIB*.   New York: Academic, 1997, ch. 8.

[6] P. Munoz, D. Pastor, and J. Capmany, "Modeling and design of arrayed waveguide gratings," *J. Lightw. Technol.*, vol. 20, no. 4, pp. 661–674, Apr. 2002.

[7] K. Okamoto, K. Moriwaki, and S. Suzuki, "Fabrication of 64×64 arrayed-waveguide grating multiplexer on silicon," *Electron. Lett.*, vol. 31, no. 3, pp. 184–185, Feb. 1995.

[8] K. Okamoto, K. Syuto, H. Takahashi, and Y. Ohmori, "Fabrication of 128-channel arrayed-waveguide grating multiplexer with a 25-GHz channel spacing," *Electron. Lett.*, vol. 32, no. 16, pp. 1474–1476, Aug. 1996.

[9] Y. Hida, Y. Hibino, T. Kitoh, Y. Inoue, M. Itoh, T. Shibata, A. Sugita, and A. Himeno, "400-channel arrayed-waveguide grating with 25 GHz spacing using 1.5%-Δ waveguides on 6-inch Si wafer," *Electron Lett.*, vol. 37, no. 9, pp. 576–577, Apr. 2001.

[10] K. Okamoto, *Fundamentals of Optical Waveguides*, 2nd ed.   New York: Academic, 2006, ch. 9.

[11] ——, "AWG technologies: Design and their applications," presented at the Optical Fiber Commun. Conf. (OFC), Baltimore, MD, 2002, SC113.

[12] K. Okamoto and H. Yamada, "Arrayed-waveguide grating multiplexer with flat spectral response," *Opt. Lett.*, vol. 20, no. 1, pp. 43–45, Jan. 1995.

[13] K. Okamoto and A. Sugita, "Flat spectral response arrayed-waveguide grating multiplexer with parabolic waveguide horns," *Electron. Lett.*, vol. 32, no. 18, pp. 1661–1662, Aug. 1996.

[14] M. R. Amersfoort, J. B. D. Soole, H. P. LeBlanc, N. C. Andreadakis, A. Rajhei, and C. Caneau, "Passband broadening of integrated arrayed waveguide filters using multimode interference couplers," *Electron. Lett.*, vol. 32, no. 5, pp. 449–451, 1996.

[15] D. Trouchet, A. Beguin, H. Boek, C. Prel, C. Lerminiaux, and R. O. Maschmeyer, "Passband flattening of PHASAR WDM using input and output star couplers designed with two focal points," presented at the Optical Fiber Commun. Conf. (OFC), Dallas, TX, 1997, ThM7.

[16] G. H. B. Thompson, R. Epworth, C. Rogers, S. Day, and S. Ojha, "An original low-loss and pass-band flattened SiO_2 on Si planar wavelength demultiplexer," presented at the Optical Fiber Commun. Conf. (OFC), San Jose, CA, 1998, TuN1.

[17] C. R. Doerr, L. W. Stulz, and R. Pafchek, "Compact and low-loss integrated box-like passband multiplexer," *IEEE Photon. Technol. Lett.*, vol. 15, no. 7, pp. 918–920, Jul. 2003.

[18] W. K. Burns, A. F. Milton, and A. B. Lee, "Optical waveguide parabolic coupling horns," *Appl. Phys. Lett.*, vol. 30, no. 1, pp. 28–30, Jan. 1977.

[19] T. Kitoh, Y. Inoue, M. Itoh, and Y. Hibino, "Low chromatic-dispersion flat-top arrayed waveguide grating filter," *Electron. Lett.*, vol. 39, no. 15, pp. 1116–1118, Jul. 2003.

[20] T. Chiba, H. Arai, K. Ohira, S. Kashimura, H. Okano, and H. Uetsuka, "Chromatic dispersion free Fourier transform-based wavelength splitters for D-WDM," presented at the Optoelectron. and Commun. Conf. (OECC), Chiba, Japan, 2000, Paper 13B2-2.

[21] C. Dragone, "Frequency routing device having a wide and substantially flat passband," U.S. Patent 5 488 680, Jan. 30, 1996.

[22] C. R. Doerr, M. A. Cappuzzo, E. Y. Chen, A. Wong-Foy, and L. T. Gomez, "Low-loss rectangular-passband multiplexer consisting of a waveguide grating router synchronized to a three-arm interferometer," *IEEE Photon. Technol. Lett.*, vol. 17, no. 11, pp. 2334–2336, Nov. 2005.

[23] C. R. Doerr, M. A. Cappuzzo, E. Y. Chen, A. Wong-Foy, L. T. Gomez, and L. L. Buhl, "Wide-band arrayed waveguide grating with three low-loss maxima per passband," *IEEE Photon. Technol. Lett.*. submitted for publication.

[24] P. A. Besse, M. Bachmann, C. Nadler, and H. Melchior, "The integrated prism interpretation of multileg Mach–Zehnder interferometers based on multimode interference couplers," *Opt. Quantum Electron.*, vol. 27, no. 10, pp. 909–920, 1995.

[25] C. R. Doerr, M. Cappuzzo, E. Laskowski, A. Paunescu, L. Gomez, L. W. Stulz, and J. Gates, "Dynamic wavelength equalizer in silica using the single-filtered-arm interferometer," *IEEE Photon. Technol. Lett.*, vol. 11, no. 5, pp. 581–583, May 1999.

[26] C. Dragone, "An $N \times N$ optical multiplexer using a planar arrangement of two star couplers," *IEEE Photon. Technol. Lett.*, vol. 3, no. 3, pp. 812–815, Sep. 1991.

[27] C. R. Doerr, "Beam propagation method tailored for step-index waveguides," *IEEE Photon. Technol. Lett.*, vol. 13, no. 2, pp. 130–132, Feb. 2001.

[28] Y. P. Li, "Optical device having low insertion loss," U. S. Patent 5 745 618, Apr. 28, 1998.

[29] A. Sugita, A. Kaneko, K. Okamoto, M. Itoh, A. Himeno, and Y. Ohmori, "Very low insertion loss arrayed-waveguide grating with vertically tapered waveguides," *IEEE Photon. Technol. Lett.*, vol. 12, no. 9, pp. 1180–1182, Sep. 2000.

[30] K. Maru, T. Chiba, M. Okawa, H. Ishikawa, K. Ohira, S. Sato, and H. Uetsuka, "Low-loss arrayed-waveguide grating with high index regions at slab-to-array interface," *Electron. Lett.*, vol. 37, no. 21, pp. 1287–1289, Oct. 2001.

[31] C. R. Doerr, R. Pafchek, and L. W. Stulz, "16-band integrated dynamic gain equalization filter with less than 2.8-dB insertion loss," *IEEE Photon. Technol. Lett.*, vol. 14, no. 3, pp. 334–336, Mar. 2002.

[32] C. R. Doerr, C. H. Joyner, and L. W. Stulz, "Integrated WDM dynamic power equalizer with potentially low insertion loss," *IEEE Photon. Technol. Lett.*, vol. 10, no. 10, pp. 1443–1445, Oct. 1998.

[33] C. R. Doerr, R. Pafchek, and L. W. Stulz, "Integrated band demultiplexer using waveguide grating routers," *IEEE Photon. Technol. Lett.*, vol. 15, no. 8, pp. 1088–1090, Aug. 2003.

[34] G. Lenz, B. J. Eggleton, C. K. Madsen, C. R. Giles, and G. Nykolak, "Optical dispersion of optical filters for WDM systems," *IEEE Photon. Technol. Lett.*, vol. 10, no. 4, pp. 567–569, Apr. 1998.

[35] S. Chandrasekhar, C. R. Doerr, and L. L. Buhl, "Flexible waveband optical networking without guard bands using novel 8-skip-0 banding filters," *IEEE Photon. Technol. Lett.*, vol. 17, no. 3, pp. 579–581, Mar. 2005.

[36] C. R. Doerr, M. Cappuzzo, L. Gomez, E. Chen, A. Wong-Foy, C. Ho, J. Lam, and K. McGreer, "Planar ligthwave circuit eight-channel CWDM multiplexer with $<$ 3.9-dB insertion loss," *J. Lightw. Technol.*, vol. 23, no. 1, pp. 62–65, Jan. 2005.

[37] D. Iazikov, C. M. Greiner, and T. W. Mossberg, "Integrated holographic filters for flat-passband optical multiplexers," presented at the Optical Fiber Commun. Conf., Anaheim, CA, 2006, Paper PDP11.

[38] G. Heise, H. W. Schneider, and P. C. Clemens, "Optical phased array filter module with passively compensated temperature dependence," in *Proc. ECOC*, Madrid, Spain, Sep. 20–24, 1998, pp. 319–320.

[39] Y. Inoue, A. Kaneko, F. Hanawa, H. Takahashi, K. Hattori, and S. Sumida, "Athermal silica-based arrayed-waveguide grating multiplexer," *Electron. Lett.*, vol. 33, no. 23, pp. 1945–1946, Nov. 1997.

[40] R. Gao, R. Gao, K. Takayama, A. Yeniay, and A. F. Garito, "Low-insertion loss athermal AWG multi/demultiplexer based on perfluorinated polymers," in *Proc. ECOC*, Copenhagen, Denmark, Sep. 8–12, 2002, pp. 1–2.

[41] J. B. D Soole, M. Schlax, C. Narayanan, and R. Pafchek, "Athermalisation of silica arrayed waveguide grating multiplexers," *Electron. Lett.*, vol. 39, no. 6, pp. 1182–1184, Aug. 2003.

[42] A. Kaneko, S. Kamei, Y. Inoue, H. Takahashi, and A. Sugita, "Athermal silica-based arrayed-waveguide grating (AWG) multiplexers with new low loss groove design," in *Proc. OFC-IOOC*, San Diego, CA, 1999, pp. 204–206.

[43] K. Takada, M. Abe, T. Shibata, and K. Okamoto, "10 GHz-spaced 1010-channel tandem AWG filter consisting of one primary and ten secondary AWGs," *IEEE Photon. Technol. Lett.*, vol. 13, no. 6, pp. 577–578, Jun. 2001.

[44] ——, "Three-stage ultra-high-density multi/demultiplexer covering low-loss fiber transmission window 1.26–1.63 μm," *Electron. Lett.*, vol. 38, no. 9, pp. 405–406, Apr. 2002.

[45] ——, "A 25-GHz-spaced 1080-channel tandem multi/demultiplexer covering the S-, C-, and L-bands using an arrayed-waveguide grating with Gaussian passbands as a primary filter," *IEEE Photon. Technol. Lett.*, vol. 14, no. 5, pp. 648–650, May 2002.

[46] ——, "5 GHz-spaced 4200-channel two-stage tandem demultiplexer for ultra-multi-wavelength light source using supercontinuum generation," *Electron. Lett.*, vol. 38, no. 12, pp. 572–573, Jun. 2005.

[47] C. R. Doerr, M. Shirasaki, and C. H. Joyner, "Chromatic focal plane displacement in the parabolic chirped waveguide grating router," *IEEE Photon. Technol. Lett.*, vol. 9, no. 5, pp. 625–627, May 1997.

[48] C. R. Doerr and C. H. Joyner, "Double-chirping of the waveguide grating router," *IEEE Photon. Technol. Lett.*, vol. 9, no. 6, pp. 776–778, Jun. 1997.

[49] C. R. Doerr, L. W. Stulz, R. Pafchek, K. Dreyer, and L. Zhang, "Potentially low-cost widely tunable laser consisting of a semiconductor optical amplifier connected directly to a silica waveguide grating router," *IEEE Photon. Technol. Lett.*, vol. 15, no. 10, pp. 1446–1448, Oct. 2003.

[50] A. Rigny, A. Bruno, and H. Sik, "Multigrating method for flattened spectral response wavelength multi/demultiplexer," *Electron. Lett.*, vol. 33, no. 20, pp. 1701–1702, Sep. 1997.

[51] C. R. Doerr, L. W. Stulz, J. Gates, M. Cappuzzo, E. Laskowski, L. Gomez, A. Paunescu, A. White, and C. Narayanan, "Arrayed waveguide lens wavelength add-drop in silica," *IEEE Photon. Technol. Lett.*, vol. 11, no. 5, pp. 557–559, May 1999.

[52] K. Okamoto, M. Okuno, A. Himeno, and Y. Ohmori, "16-channel optical add/drop multiplexer consisting of arrayed-waveguide gratings and double-gate switches," *Electron. Lett.*, vol. 32, no. 16, pp. 1471–1472, Aug. 1996.

[53] T. Saida, A. Kaneko, T. Goh, M. Okuno, A. Himeno, K. Takiguchi, and K. Okamoto, "Athermal silica-based optical add/drop multiplexer consisting of arrayed waveguide gratings and double gate thermo-optical switches," *Electron. Lett.*, vol. 36, no. 6, pp. 528–529, Mar. 2000.

[54] A. Sugita, K. Jinguji, N. Takato, K. Katoh, and M. Kawachi, "Bridge-suspended thermo-optic phase shifter and its application to silica-waveguide optical switch," in *Proc. IOOC*, 1989, p. 58.

[55] R. Kasahara, M. Yanagisawa, A. Sugita, T. Goh, M. Yasu, A. Himeno, and S. Matsui, "Low-power consumption silica-based 2×2 thermooptic switch using trenched silicon substrate," *IEEE Photon. Technol. Lett.*, vol. 11, no. 9, pp. 1132–1134, Sep. 1999.

[56] C. R. Doerr, L. W. Stulz, M. Cappuzzo, E. Laskowski, A. Paunescu, L. Gomez, J. V. Gates, S. Shunk, and A. E. White, "40-wavelength add-drop filter," *IEEE Photon. Technol. Lett.*, vol. 11, no. 11, pp. 1437–1439, Nov. 1999.

[57] C. R. Doerr, L. W. Stulz, R. Monnard, M. Cappuzzo, L. Gomez, E. Laskowski, A. Paunescu, S. Shunk, O. A. Clarke, A. Bing, and R. K. Vora, "40-wavelength planar channel-dropping filter with improved crosstalk," *IEEE Photon. Technol. Lett.*, vol. 13, no. 9, pp. 1008–1010, Sep. 2001.

[58] C. R. Doerr, L. W. Stulz, R. Pafchek, and S. Shunk, "Compact and low-loss manner of waveguide grating router passband flattening and demonstration in a 64-channel blocker/multiplexer," *IEEE Photon. Technol. Lett.*, vol. 14, no. 1, pp. 56–58, Jan. 2002.

[59] C. R. Doerr, L. W. Stulz, M. Cappuzzo, L. Gomez, A. Paunescu, E. Laskowski, S. Chandrasekhar, and L. Buhl, "2 × 2 wavelength-selective cross connect capable of switching 128 channels in sets of eight," *IEEE Photon. Technol. Lett.*, vol. 14, no. 3, pp. 387–389, Mar. 2002.

[60] C. R. Doerr, L. W. Stulz, D. S. Levy, L. Gomez, M. Cappuzzo, J. Bailey, R. Long, A. Wong-Foy, E. Laskowski, E. Chen, S. Patel, and T. Murphy, "Eight-wavelength add-drop filter with true reconfigurability," *IEEE Photon. Technol. Lett.*, vol. 15, no. 1, pp. 138–140, Jan. 2003.

[61] C. R. Doerr, L. W. Stulz, D. S. Levy, R. Pafchek, M. Cappuzzo, L. Gomez, A. Wong-Foy, E. Chen, E. Laskowski, G. Bogert, and G. Richards, "Wavelength add-drop node using silica waveguide integration," *J. Lightw. Technol.*, vol. 22, no. 12, pp. 2755–2757, Dec. 2004.

[62] A. M. Weiner, J. P. Heritage, and E. M. Kirshner, "High-resolution femtosecond pulse shaping," *J. Opt. Soc. Amer. B, Opt. Phys.*, vol. 5, no. 8, pp. 1563–1572, Aug. 1988.

[63] K. Okamoto, T. Kominato, H. Yamada, and T. Goh, "Fabrication of frequency spectrum synthesiser consisting of arrayed-waveguide grating pair and thermo-optic amplitude and phase controllers," *Electron. Lett.*, vol. 35, no. 9, pp. 733–734, Apr. 1999.

[64] A. M. Weiner, J. P. Heritage, and R. N. Thurston, "Synthesis of phase coherent, picosecond optical square pulses," *Opt. Lett.*, vol. 11, no. 3, pp. 153–155, Mar. 1986.

[65] S. Kawanishi, H. Takara, K. Morioka, O. Kamatani, and M. Saruwatari, "200 Gb/s, 100 km time-division-multiplexed optical transmission using supercontinuum pulses with prescaled PLL timing extraction and all-optical demultiplexing," *Electron. Lett.*, vol. 31, no. 10, pp. 816–817, May 1995.

[66] K. Takiguchi, K. Okamoto, T. Kominato, H. Takahashi, and T. Shibata, "Flexible pulse waveform generation using a silica waveguide-based spectrum synthesis circuit," *Electron. Lett.*, vol. 40, no. 9, pp. 537–538, Apr. 2004.

[67] C. R. Doerr, S. Chandrasekhar, P. J. Winzer, A. R. Chraplyvy, A. H. Gnauck, L. W. Stulz, R. Pafchek, and E. Burrows, "Simple multichannel optical equalizer mitigating intersymbol interference for 40-Gb/s nonreturn-to-zero signals," *J. Lightw. Technol.*, vol. 22, no. 1, pp. 249–251, Jan. 2004.

[68] C. R. Doerr, P. J. Winzer, G. Raybon, L. L. Buhl, M. A. Cappuzzo, A. Wong-Foy, E. Y. Chen, L. T. Gomez, and M. Duelk, "A single-chip optical equalizer enabling 107-Gb/s optical non-return-to-zero signal generation," in *Proc. Eur. Conf. Opt. Commun.*, 2005, pp. 13–14. post deadline paper.

[69] C. K. Madsen and J. H. Zhao, *Optical Filter Design and Analysis*. Hoboken, NJ: Wiley, 1999.

[70] K. Takiguchi, K. Jinguji, K. Okamoto, and Y. Ohmori, "Variable group-delay dispersion equalizer using lattice-form programmable optical filter on planar lightwave circuit," *IEEE J. Sel. Topics Quantum Electron.*, vol. 2, no. 2, pp. 270–276, Jun. 1996.

[71] C. R. Doerr, L. W. Stulz, S. Chandrasekhar, and R. Pafchek, "Colorless tunable dispersion compensator with 400-ps/nm range integrated with a tunable noise filter," *IEEE Photon. Technol. Lett.*, vol. 15, no. 9, pp. 1258–1260, Sep. 2003.

[72] D. M. Marom, C. R. Doerr, M. A. Cappuzzo, E. Y. Chen, A. Wong-Foy, L. T. Gomez, and S. Chandrasekhar, "Compact colorless tunable dispersion compensator with 1000-ps/nm tuning range for 40-Gb/s data rates," *J. Lightw. Technol.*, vol. 24, no. 1, pp. 237–241, Jan. 2006.

[73] C. R. Doerr, R. Blum, L. L. Buhl, M. A. Cappuzzo, E. Y. Chen, A. Wong-Foy, L. T. Gomez, and H. Bulthuis, "Colorless tunable optical dispersion compensator based on a silica arrayed-waveguide grating and a polymer thermooptic lens," *IEEE Photon. Technol. Lett.*, vol. 18, no. 11, pp. 1222–1224, Jun. 2006.

[74] C. R. Doerr, S. Chandrasekhar, L. L. Buhl, M. A. Cappuzzo, E. Y. Chen, A. Wong-Foy, and L. T. Gomez, "Optical dispersion compensator suitable for use with non-wavelength-locked transmitters," *J. Lightw. Technol.*, vol. 24, no. 1, pp. 166–170, Jan. 2006.

[75] C. R. Doerr, S. Chandrasekhar, M. A. Cappuzzo, A. Wong-Foy, E. Y. Chen, and L. T. Gomez, "Four-stage Mach–Zehnder-type tunable optical dispersion compensator with single-knob control," *IEEE Photon. Technol. Lett.*, vol. 17, no. 12, pp. 2637–2639, Dec. 2005.

[76] A. Sneh and C. R. Doerr, "Indium phosphide-based photonic circuits and components," in *Integrated Optical Circuits and Components*. New York: Marcel Dekker, 1999, ch. 7.

[77] L. Eldada and L. W. Shacklette, "Advances in polymer integrated optics," *IEEE J. Sel. Topics Quantum Electron.*, vol. 6, no. 1, pp. 54–68, Jan./Feb. 2000.

[78] B. E. Little, S. T. Chu, P. P. Absil, J. V. Hryniewicz, F. G. Johnson, F. Seiferth, D. Gill, V. Van, O. King, and M. Trakalo, "Very high-order microring resonator filters for WDM applications," *IEEE Photon. Technol. Lett.*, vol. 16, no. 10, pp. 2263–2265, Oct. 2004.

[79] R. C. Alferness, "Titanium-diffused lithium niobate waveguide devices," in *Guided-Wave Optoelectronics*, 2nd ed. New York: Springer-Verlag, 1990, ch. 4.

[80] W. Bogaerts, R. Baets, P. Dumon, V. Wiaux, S. Beckx, D. Taillaert, B. Luyssaert, J. Van Campenhout, P. Bienstman, and D. Van Thourhout, "Nanophotonic waveguides in silicon-on-insulator fabricated with CMOS technology," *J. Lightw. Technol.*, vol. 23, no. 1, pp. 401–412, Jan. 2005.

Christopher Richard Doerr (M'97) received the B.S. degree in aeronautical/astronautical engineering and the B.S., M.S., and Ph.D. degrees in electrical engineering from the Massachusetts Institute of Technology (MIT), Cambridge. His Ph.D. thesis on constructing a fiber-optic gyroscope with noise below the quantum limit was supervised by Prof. H. Haus.

In 1991, he was with MIT on an Air Force ROTC scholarship and earned his pilot wings at Williams AFB, Mesa, AZ. Since 1995, he has been with Lucent Technologies, Bell Laboratories, Holmdel, NJ, where his research has focused on integrated devices for optical communication. In 2000, he was promoted to Distinguished Member of Technical Staff.

Dr. Doerr is the Editor-in-Chief of IEEE PHOTONICS TECHNOLOGY LETTERS, is an elected member of the LEOS Board of Governors, and was a subcommittee chair for OFC 2005. He received the OSA Engineering Excellence Award in 2002.

Katsunari Okamoto (M'85–SM'98–F'03) was born in Hiroshima, Japan, on October 19, 1949. He received the B.S., M.S., and Ph.D. degrees in electronics engineering from University of Tokyo, Tokyo, Japan, in 1972, 1974, and 1977, respectively.

In 1977, he was with Ibaraki Electrical Communication Laboratory, Nippon Telegraph and Telephone Corporation (NTT), Ibaraki, Japan, and was engaged in research on transmission characteristics of multimode, dispersion-flattened single-mode single-polarization (PANDA) fibers, and fiber-optic components. He proposed for the first time the dispersion-flattened fiber (DFF) and succeeded in the fabrication of DFF that had chromatic dispersion less than +/-1 ps/km/nm over a wide spectral range. From September 1982 to September 1983, he was a Guest Researcher with the Optical Fiber Group, Southampton University, Southampton, U.K., where he was engaged in research on birefringent optical fibers. From October 1987 to October 1988, he was an Associate Professor with the Research Center for Advanced Science and Technology (RCAST), University of Tokyo, with Dr. E. A. J. Marcatili from AT&T Bell Laboratories. He was a Guest Professor of the endowed chair at RCAST. They studied the influence of nonlinear optical effects on propagation characteristics of optical fibers. Along with research activities, they taught electromagnetic theory, optoelectronics, and fiber optics at the Electronics and Applied Physics Department. Since 1990, he has been working on the analysis and the synthesis of guided-wave devices and the computer-aided-design (CAD) and fabrication of silica-based planar lightwave circuits (PLCs) at Ibaraki R&D Center, NTT Photonics Laboratories. He developed a CAD tool based on the beam propagation method and a FEM waveguide and stress analyses. The design tool for arrayed waveguide grating (AWG) filter is widely utilized in the NTT Photonics Laboratory and its subsidiary company (NEL). He has developed a 256 x 256 star coupler, various kinds of AWGs, ranging from eight-channel 300-nm-spacing AWGs to 128-channel 25-GHz AWGs, flat spectral response AWGs, and integrated-optic reconfigurable add/drop multiplexers. Two hundred- to 50-GHz-spacing AWGs are now widely used in commercial WDM systems. In 2003, he started Okamoto Laboratory Ltd. Okamoto Laboratory is an R&D consulting company that deals with the custom design of optical fibers and functional planar lightwave circuits. Since July 2006, he has been a Professor of electrical and computer engineering at the University of California, Davis (UC Davis). He has published more than 220 papers in technical journals and international conferences. He authored and coauthored eight books including *Fundamentals of Optical Waveguides*. His research includes passive and active photonics devices for high-performance all-optical networks.

Dr. Okamoto is a member of the Optical Society of America and the Institute of Electronics, Information, and Communication Engineers of Japan.